Aero-Hydro-Elastic Simulation Platform for Wave Energy Systems and floating Wind Turbines

Kallesøe, Bjarne Skovmose

Publication date:
2011

Document Version
Publisher's PDF, also known as Version of record

Aero-Hydro-Elastic Simulation Platform for Wave Energy Systems and floating Wind Turbines

Risø-R-Report

Bjarne S. Kallesøe
Risø-R-1767(EN)
January 2011

Risø DTU
National Laboratory for Sustainable Energy

Author: Bjarne S. Kallesøe
Title: Aero-Hydro-Elastic Simulation Platform for Wave Energy Systems and floating Wind Turbines
Division: Wind Energy Division

Abstract (max. 2000 char.):
This report present results from the PSO project 2008-1-10092 entitled Aero-Hydro-Elastic Simulation Platform for Wave Energy Systems and floating Wind Turbines that deals with measurements, modelling and simulations of the world's first combined wave and wind energy platform. The floating energy conversion platform, Poseidon, is own and operated by Floating Power Plant A/S. The platform has been operating for two test periods; one period where it was operating as a wave energy conversion platform only and one period where the three turbines was mounted and the platform operated as a combined wind and wave energy platform. The PSO project has equipped the platform with comprehensive measurements equipment for measuring platform motion, wave and wind conditions and turbine loads. Data from the first test period has been used for determine if the turbine could be mounted on the platform. Preliminary analysis of data from the second test period indicates that the platform is suitable as wind turbine foundation and that the turbines reduce the platform motion.

Risø-R-1767(EN)
January 2011

ISSN 0106-2840
ISBN 978-87-550-3883-7

Contract no.:
PSO-2008-1-10092

Group's own reg. no.:
PSP-1110066-01

Sponsorship:

Cover :

Pages: 57
Tables:
References:

Information Service Department
Risø National Laboratory for Sustainable Energy
Technical University of Denmark
P.O.Box 49
DK-4000 Roskilde
Denmark
Telephone +45 46774005
bibl@risoe.dtu.dk
Fax +45 46774013
www.risoe.dtu.dk

Contents

1 Summary

This report presents results from the PSO project 2008-1-10092 entitled Aero-Hydro-Elastic Simulation Platform for Wave Energy Systems and floating Wind Turbines that deals with measurements, modeling and simulations of the world's first combined wave and wind energy platform, called Poseidon. The Poseidon project combines wind and wave energy. The concept is owned by Floating Power Plant A/S and is based on a large stable triangular floating foundation, which works both as a floating platform for a patented wave energy concept and wind turbines. The wave energy part of the concept is a multi absorber system, where the waves force the dynamically ballasted floats up and down. The floats activate hydraulic cylinders that pump water through a water turbine, driving an electric generator. The wind energy part of the concept utilizes the large stable platform as a floating foundation for wind turbines. The present version of Poseidon is a 37 meter wide off-shore test plant with an expected wave energy effect on 140 kW and three 11 kW wind turbines.

The PSO project has equipped the platform with comprehensive measurements equipment for measuring platform motion, wave and wind conditions and turbine loads. The platform has been tested at sea for two periods; first one period where it was operating as a wave energy conversion platform only and next one period where it was operating as a combined wind and wave energy conversion platform. Data from the first test period has been used to quantify the extra loading that the wind turbines will encounter because of the floating platform. This analysis lead to a go-ahead for mounting the turbines on the platform and continuation with the second test phase operating as an combined wind and wave energy conversion platform.

Analysis of data from the second test phase shows that the platform is useable as a wind turbine foundation. The analysis shows that the turbine tower loads increase with increased platform motion, as expected, and that the blade loads one the other hand are not affected by the platform motion. Furthermore the analysis indicates that the wind turbines reduce the platform pitch motion, properly because of the large aerodynamic damping for longitudinal rotor motion of these stall regulated wind turbines.

To model and simulate the platform the aeroelastic code HAWC2 developed at Risø for computing wind turbine loads is integrated with DHI's radiation/diffraction floating body analysis tool, WAMSIM. By combining two validated codes a very strong tool for analyzing new advance concepts as the Poseidon platform is achieve. The first validation computations shows very promising results.

The work in this project will be continued in the PSO project *Poseidon 2*. The test platform will be upgraded and teste for one more period at sea. The data from all measurement periods will be further analyzed, focusing on e.g. direction stability of the platform, turbine loading, platform-turbine interaction. The numerical simulation platform will be further validated against the measurements and used to simulate and analysis some of the events found in the measurements. Finally the simulation tool will be used to look into upscaling issues for such a combined wave and wind energy conversion concept.

2 Introduction

This report present results from the world's first operating floating combined wave and wind energy conversion platform. The high focus on offshore renewable energy and the limit number of sits in shallow waters, which are suited for the conventional bottom mounted offshore wind turbine concept has directed focus towards floating concepts. The high cost of offshore installations motivates the idea of combining several renewable energy converters to share the expensive mooring system and grid integration. One option is to combine wind and wave energy converters.

Wave energy conversion has become a growing field in the renewable energy sector. It first attracted interest in the 1970s, when Stephen Salter from the University of Edinburgh devised a device that converted the motion of waves into electricity [1]. Over the past few decades, both scientific and industrial communities have produced a great interest to wave energy, and many wave energy conversion devices have been developed to extract the hydro-kinetic and hydro-potential energy from wave motion. Wave energy conversion devices in the market can be classified into two major categories based on their orientation and functionality: Turbine-type or oscillating water column converters (e.g. LIMPET) and buoy-type or point absorber converters (e.g. Wave Star). A systematic and comprehensive overview of wave energy converters can be found in [2, 3].

Wind energy has until now been one of the most successful renewable energy sources. The technology for conversion of wind energy into electrical energy has converged into a few types. Although the three bladed horizontal axis turbine with a gearbox (known as the Danish concept) has been the most favoured design, a two bladed design has also had some success, especially for smaller turbines. One of the main development areas in the expansion of wind energy is to establish offshore wind turbine parks [4]. The offshore wind quality is superior to onshore for most sites and the offshore wind turbine structures do not interfere on noise and visual impacts. The present offshore wind turbine technology, with bottom fixed foundations, allows only water depths up to ≈ 30 m. To overcome the water depth limit on wind turbine sites, the floating wind turbine concepts have been developed. The Hywind project is a generic representative of this technology, and consists of a large spar-buoy filled with ballast at the bottom of the buoy and a conventional turbine on the top. The system is stabilized by the ballast in the bottom of the buoy and kept in position by three anchors. Another floating wind turbine concept is the SWAY, which has an integrated spar-buoy turbine concept stabilized and kept in position by a tension leg and a gravity anchor.

Building large offshore constructions, such as floating wave and wind energy conversion systems, including anchor system and power connection are very expensive. The high construction and infrastructure costs motivate the idea of combining wind and wave energy conversion systems, and thereby share common components, such as power connection and anchor system. Furthermore combined systems will create some synergy effects: wave energy conversion system may reduce the wave excitation of a floating foundation, while wind turbines may damp the motion of the floating foundation, and wind and wave energy intensity will have some phase shift in time and the total power production will be smoothing.

The Poseidon project combines wind and wave energy. The concept is owned by Floating Power Plant A/S and is based on a large stable triangular floating foundation, which works both as a floating platform for a patented wave energy concept and wind turbines. The wave energy part of the concept is a multi absorber system, where the waves force

the dynamically ballasted floats up and down. The floats activate hydraulic cylinders that pump water through a water turbine, driving an electric generator. The wind energy part of the concept utilizes the large stable platform as a floating foundation for wind turbines. The present version of Poseidon is a 37 meter wide off-shore test plant with an expected wave energy effect on 140 kW (Figure 1) and three 11 kW wind turbines.

This paper presents results from the demonstration plant. Chapter two describe the general experiences with operation of the platform. Chapter three deals with the first test period, where the platform without wind turbines was tested at sea, this chapter also presents the pre turbine load analysis conducted before the turbine could be mounted on the platform. Chapter four presents the results from second test period, where the platform was tested at sea with the turbines on. Chapter five present the numerical modeling effort in the project and finally chapter six conclude the work.

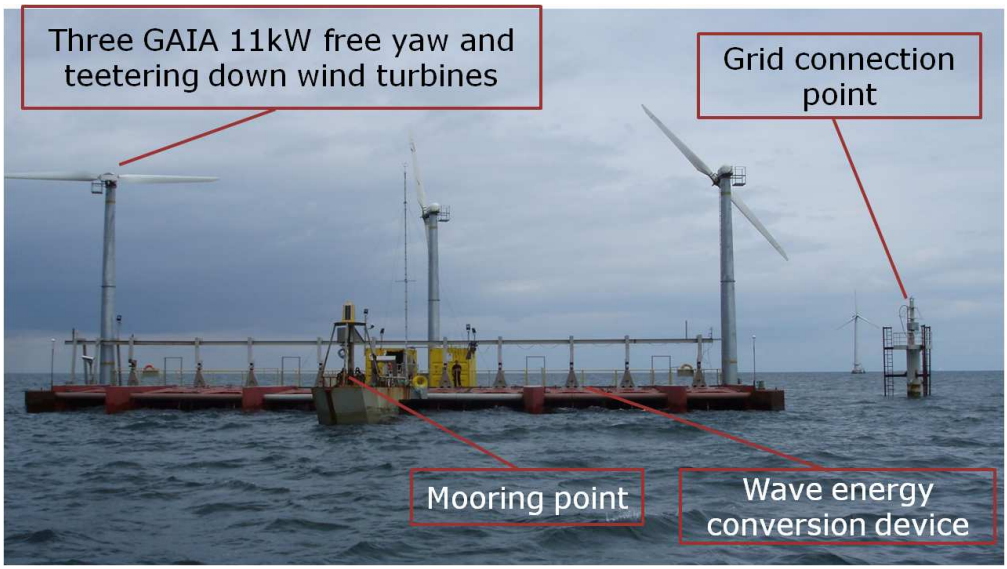

Figure 1. The Poseidon demonstration platform at sea.

3 General introduction and operational experiences

By Floating Power Plant

A floating foundation which works as a platform for extracting energy from both wind and wave power. That is Poseidon - wind and wave in one.

Poseidon is developed by Floating Power Plant A/S, (FPP) a Danish company holding all rights to develop and build the patented Poseidon concept. Today FPP runs not only Denmarks biggest off-shore test plant for wave energy in operation but also the only floating foundation for wind turbines.

The Poseidon concept consists of three main technologies:

1. An anchored floating off-shore platform that can survive the extreme conditions. The platform can rotate 360 degrees depending on the wave direction.
2. A wave energy concept (multi absorber) for extraction of wave energy.
3. A stable (low movement) floating platform for standard Off-shore wind turbines.

3.1 Development history

During the last 12 years FPP has managed to develop the concept from idea, through design and modeling to test of various scale models. A short summary of test activities are listed below. Between these tests development, engineering and capital raising activities has been performed.

One of FPP and is competitors (both in wave and floating off-shore wind) challenges in the development of a completely new technology is the lack of proven development, design and simulation tools.

A constant interaction between empirical scaled test and development off tools is therefore necessary. This to verify concepts, simulations and tools. Seen from a developers perspective this PSO project is crucial in regard to the development of the necessary tools and know how, but just as important, to validate /calibrate the tools so that they can be used and "trusted" when scaling up to commercial facilities.

3.2 Off-Shore tests - operational experiences

This PSO project has covered simulation, measurement, data analysis and simulation validation in regard to wind turbines on floating foundations for two off-shore periods.

The reason behind FFPs construction of a large scale off-shore test facility is to test, learn and verify/validate but with a broader focus than the PSO project. Focus has been on all three of FPPs main technology areas (listed below), this from specific test of technology to experiences with construction, installation, maintenance, daily operation, grid connection, safety, control systems, etc.

Year	PSO	Nr.	Test activity	
1998	No	P1	Conceptual design and test in 3D basins of a 2,4 meter (wave front) floating power plant at AAU.	
2000	No	P2	Two empirical wave flume tests phases of different floats designs at DHI.	
2002	No	P3	Test of a 8,4 meter (wave front) model with wind turbines was tested in a 3D basin at DHI.	
2008/ 2009	Yes	*P4.1*	*Off-shore test phase 1.* Off-shore test of a 37 meter (wave front) floating power plant was initiated. The first test was performed without the wind turbines installed.	
2010	Yes	*P4.2*	*Off-shore test phase 2.* Further off-shore test of a 37 meter (wave front) floating power plant. This second test was performed with 3 grid connected wind turbines installed.	
2010	No	P5	Wave flume test of an improved PTO system for the wave energy device.	
			Planned tests	
2011	Yes	*P4.3*	Off-shore test phase 3 Further off-shore test of the 37 meter (wave front) floating power plant. This third and final off-shore test will be performed with 3 grid connected wind turbines (increased measurement program) and further test with a grid connect PTO system from the wave energy device.	
2011	No	P6	3D basin test of key parameters concerning scaling and stability of the platform- stability. The test result will be integrated in the numeric model.	

Figure 2. Table showing Poseidon's development history.

1. An anchored floating off-shore platform that can survive the extreme conditions. The platform can rotate 360 degrees depending on the wave direction.
2. A wave energy concept (multi absorber) for extractions of wave energy.
3. A stable (low movement) floating platform for standard Off-shore wind turbines.

P37 has been designed as a flexible and disconnectable facility. The goal was to create a platform that could be integrated as a part of a controlled learning loop (se figure 1). P37 can therefore easily be transported back to harbor and prepared for new tests without removing the anchoring system and electrical infrastructure. Currently two off-shore test phases has been completed with P37. Seen in perspective to this PSO project the process has been:

Pre test phase 1 and load calculations of the GAIA wind turbines.

Off-shore test 1 Re-simulation and validation of the loads and performance of the GAIA wind turbines.

Post test phase 1/ Pre test phase 2 Re-simulation and validation of the loads and performance of the GAIA wind turbines.

Off-shore test 2 Operation and measurements with the three grid connected wind turbines installed to verify changes in stability, loads, survivability, platform movements, etc.

Post test phase 2 Data analysis, platform and wind turbine performance, simulation validation, etc.

The focus of this PSO project is on the more analytic part off off-shore operation which will be addressed in the coming chapters of this report. Some more general experiences with developing wind turbines on floating foundation are:

- *The more you can test on land /in harbor the better.*
  FPP has identified several issues during pre-test that would have caused delays, been costly and a few times critical during pre-test. An example is an unwanted resonance situation in the rear wind turbine. Simulations and on-land tests (the wind turbines has been in full production on the platform on land) indicated and measured no problems with resonance. After craning out the platform, installing the wind turbines again and during a full production harbor test an unwanted resonance situation was identified in the rear wind turbine foundation. This caused a delay
- *Combine measurement and visual means.*
  This to increase understanding, improve operation and in developing new ideas. FPP has spend many hours off-shore during test runs on an in principle unmanned unit. The experiences. Knowhow and spin offs here from are priceless.
- *Secure safe access and service materials close by.*
  The fact that P37 turns 360 degrees, thereby creating a safe zone behind the platform for transfer(the wave energy devise absorbs the waves) and that the platform contains full facility workshop and office has increased safety and down time on wind turbines and the wave energy device significantly.
- *Use well tested solutions and test them again.*
  FPP has teamed up with some of the world's leading specialist in the development and design process. The main reason for this is to learn as much as possible from businesses with proven off-shore track records. Survivability and safety is essential. Developers should however still be critical when applying technology /concept from other businesses, and secure that they are retested and verified .e.g. in basin tested before installing off-shore.

3.3 Going forward

A more holistic view of the results from the first two off-shore test phases are very positive seen from FPPs perspective. Both the operational and analytical results confirm that the platform can be used as floating foundation for wind turbines. The challenge going forward and scaling up to MW facilities lies in increasing stability even further, addressing fatigue and the wind turbine constellation on the platform.

These issues will for example be addressed in:

- The third and final off-shore test which have receive further support from the PSO program.

- Further development of the platform design and numeric models.
- Further 3D basin test to verify models, concepts and scaling parameters.

The overall strategic goal is to launch the first commercial power plant late 2013 or early 2014. The most interesting market to launch the Poseidon technology is in the southern part of Europe or on the Americas. Close relations to relevant parties has been established during the last 8 month and the foundation for commercial utilization is thereby in place.

3.4 Summary

From a developer and industry point this completed PSO project has aided and aid significantly in the development of the necessary know how, tools and validation for moving the industry and FPP forward.

The process is not finished and there is need for further development and validation.

The approved PSO support for RISØ-DTU and DHI for further development during FPP's third off-shore test phase is very positive seen from the industry point off view.

4 Results from first measurement campaign

By RisøDTU

This chapter deals with the first test period, where the platform was tested without turbines. An analysis of the expected turbine loads are also shown. This analysis has been used to approve the test with turbines on the platform.

4.1 Platform Motion

This section presents measurements from the Poseidon demonstration platform. The measured platform motion is compared to computed eigenfrequencies of the platform.

From 4/8-2008 to 17/2-2009 the Poseidon demonstration plant has been tested at sea without the wind turbines. This test period has been used to adjust the operation of the wave energy conversion system and to collect data describing the wave and wind conditions together with the motion of the platform. The data includes: i) one three-axis accelerometer in each of the three turbine foundations, ii) roll and pitch angle measurements in one turbine foundation, iii) angular position of one wave energy extracting float, iv) wind speed in three directions. All sensors are sampled with 32 Hz. Wave height, wave period, current speed, and position of the platform have been recorded with 20 and 10 minutes sequences respectively.

Figure 3 and 4 show the 10 minute statistics for the platform roll and pitch, together with the significant wave hight. The shown period is the one with the highest significant

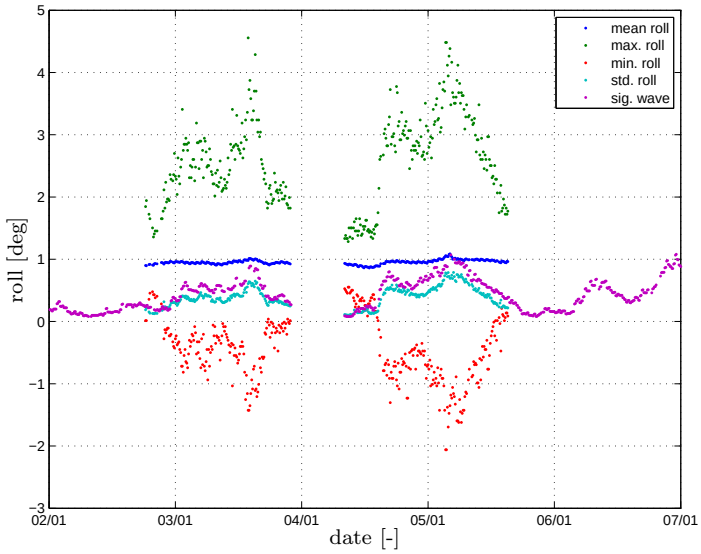

Figure 3. Statistics for roll of platform together with the significant wave height, positive = starboard down.

wave heights during the measurements. The platform motion follows the significant wave height closely, having roll and pitch amplitudes on up to 3 deg where the significant wave height is largest. The offset of ≈ 1 deg can be adjusted by trimming the platform with ballast water. Trimming the platform is a part of the optimization process of the wave energy conversion system.

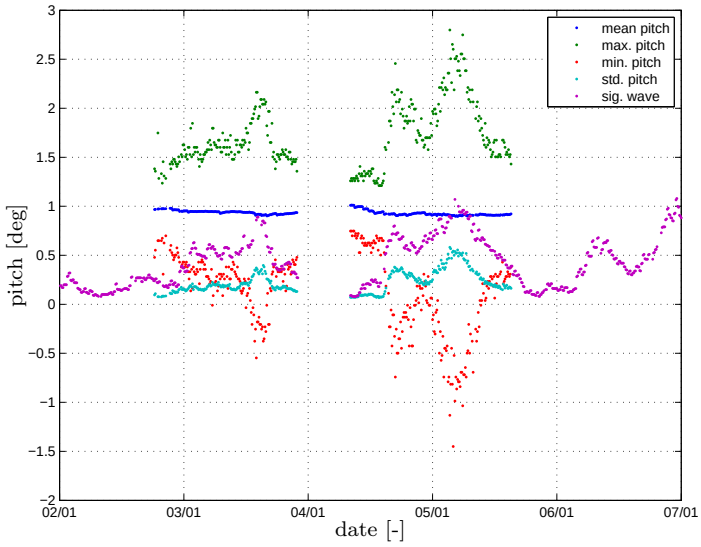

Figure 4. Statistics for pitch of platform together with the significant wave height, positive = bow down.

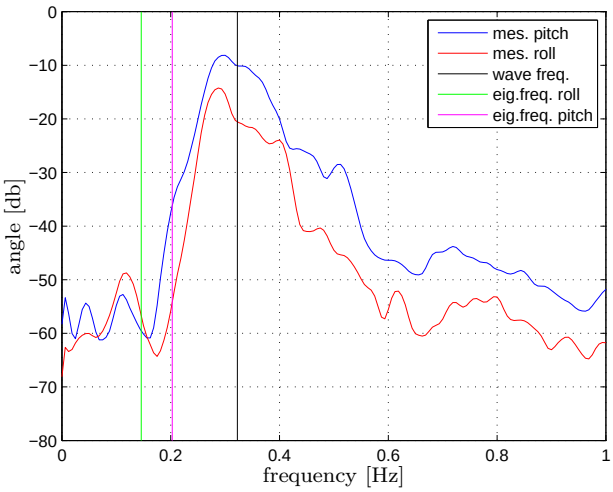

Figure 5. Power spectrum of measured pitch and roll angle of platform at 0:00 to 0:35 the 3th January 2009. Measured wave frequency and computed platform eigenfrequencies are also shown.

Figure 5 shows the power spectrum of roll and pitch of the platform.

The eigenfrequencies of the platform have been computed using the time-domain code for vessel motion analysis, WAMSIM, developed by DHI. WAMSIM relies on the industry standard radiation-diffraction program WAMIT to solve the first-order radiation-diffraction problem in the frequency domain over bodies discritized with quadrilateral panels. WAMSIM takes the hydrodynamic quantities into the time domain through a Fourier transform and combines them with incident wave forcing, wind forcing, forcing from a non-linear mooring system and viscous damping forces in order to solve the equations of motions for the body in 6 degree of freedom. The method is further described and validated in [5] and [6].

The panel representation of the wave energy converter is shown in Figure 6. Decay test analyzes have been conducted in the numerical WAMSIM model. The wave energy

converter has been given an initial displacement away from equilibrium and the oscillating, decaying motion back to equilibrium analyzed with respect to its frequency. The catenary anchor chain mooring system of the wave energy converter is included in the model. While eigenfrequencies in heave, roll and pitch are dominated by the mass and shape of the floating platform itself, the surge eigenfrequency is governed by the mooring system. Table 1 shows the computed eigenfrequencies. The power spectrum for the

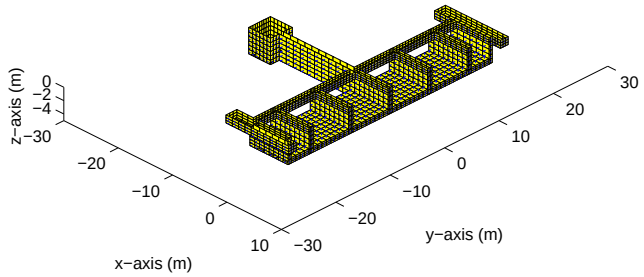

Figure 6. Panel representation of floating wave energy converter, Poseidon.

mode	frequency
surge	0.017 Hz
heave	0.098 Hz
roll	0.146 Hz
pitch	0.203 Hz

Table 1. Eigenfrequencies of the platform computed by the WAMSIM model.

platform roll shows a small peak close to the natural roll frequency (0.146 Hz) but the major frequency content is at ≈0.3 Hz. The main part of the frequency contents of the pitch motion is also at ≈0.3 Hz. The wave frequency corresponds well to the main peaks in the power spectrum of platform roll and pitch showing that the platform motion is dominated by the waves. Figure 7 shows the zero crossing frequency from all the wave statistics. It is seen that the wave periods are normally higher than the eigenfrequencies of the platform. The wave period is likely to coincide with the platform eigenfrequency only for very extreme events. No such events have so far occurred during the testing of the wave energy converter.

4.2 Special Issues for Turbine on Floating Foundation

Mounting wind turbines on a floating foundation, such as the Poseidon demonstration platform, imposes a series of known issues compare to turbines with fixed foundations.

Issue 1 Generally, for all turbine concepts the roll and pitch angle of the platform tilt the tower, whereby the center of gravity of the tower top mass is offset from the

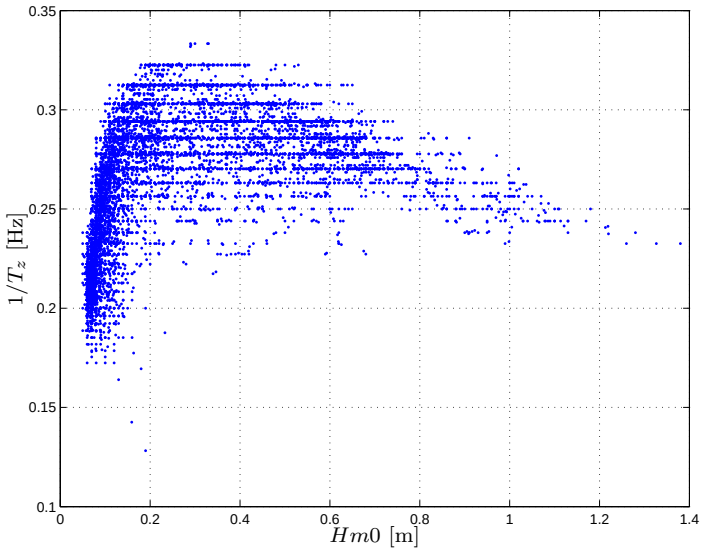

Figure 7. Zero crossing frequency $1/T_z$ of the waves as function of significant wave height $Hm0$.

tower bottom. This offset of tower top mass together with gravity force impose an increased tower bottom bending moment.

Issue 2 On pitch controlled turbine, the pitch controller will make the system unstable if not redesigned [7]. This is because when the turbine tilts forward, it experiences a relatively higher wind speed and the pitch controller reduces the trust. When the tower tilts backward the relative wind speed decreases and the pitch controller increases the trust. All in all, this will result in a negative damped motion, if the pitch control doesn't disregard wind speed changes imposed by platform motion. This is not an issue for the turbines on the Poseidon demonstration platform, since these are fixed pitch stall regulated turbines.

Issue 3 Special for the turbines on the Poseidon demonstration platform is that they have a free yaw system, meaning that the nacelle is free to rotate 360 deg and the alignment with the wind is only insured by the aerodynamic forces. The center of gravity of the tower top mass is offset from the yaw bearing's center of rotation, as it is located between tower and rotor. When the tower is tilted this offset of center of gravity together with the gravity force will cause a turning moment on the nacelle. Since this turbine has a free yaw system, the turning moment can change the yaw settings and create a misalignment between wind and turbine.

4.3 The Wind Turbine

Three 11 kW Gaia wind turbines (Figure 8) will be mounted on the Poseidon platform. Table 2 shows a short list of specifications for the turbines. The Gaia turbine has two blades with a teetering hub[1] and a free yaw system. The turbine runs at a fixed speed, having a gearbox and an asynchronous generator. It has a fixed pitch and uses stall to limit the power production.

Table 3 shows the resonance frequencies of the turbine.

[1]The blades are fixed to each other but hinge in a bearing such that they can make rigid body rotation out of the rotor plane.

Figure 8. Picture of a Gaia turbine, similar to the ones which will be mounted on the Poseidon platform.

Rotor diameter	13 m
Tower hight	12 m
Tower top mass	900 kg
Rated power	11 kW
Cut in wind speed	3.5 m/s
Cut out wind speed	25 m/s
Rated wind speed	9.5 m/s
Rotation speed	56 rpm

Table 2. Specifications for the Gaia wind turbine.

The yaw bearing has a friction resistance of 20 Nm. It is known that this friction has a large stabilizing effect on the yaw/teeter stability of the turbine, and therefore it is important to include that in the model. The teeter bearing is model with a linear stiffness of 5000 Nm/rad and a damping of 1000 Nms/rad. The stiffness is estimated from previous works done on a similar turbine at Risø [8, 9] and the damping is estimated based on a measure of the damping of the teeter bearing rubber bushing.

Description	Gaia	Meas.	HAWC2
rigid flap		0.75	0.76
rigid edge		1.5	1.61
lateral tower	3.06		2.94
longitudinal tower	3.06		3.37
1st flap (sym. Flap)		3	3.62
2nd flap		5.75	5.48
1st edge			6.69
3th flap		10.25	9.67
4th flap		15.75	15.65
5th flap			16.85
6th flap			18.56
7th flap			20.31
8th flap			21.06
2nd lateral tower	26		23.19

Table 3. Standstill resonance frequencies of the Gaia turbine. First column: data provided by Gaia, second column: measurements on blades only, third column: results from the HAWC2 model, all frequencies in Hz.

4.3.1 Aeroelastic Wind Turbine Simulation

The turbine is modeled in the aeroelastic time simulation code HAWC2 [10]. The aeroelastic model is used to analyze the effect of the platform motion on the turbines. In this section, first normal operation conditions are simulated to create a basis for the comparison and then the effect of the platform motion on the tower bottom bending moment and the effect on the yaw and teeter motion are analyzed.

Normal Operation Figure 9 and 10 show the response of tower bottom bending moment, teeter and yaw to normal operation in turbulent wind condition corresponding to SWT class I in the IEC-standard 61400-2. The tower bottom bending moment (Figure 9) increases monotonic with the wind speed, this is characteristic for a stall regulated turbine, as the Gaia, since the trust on the rotor continues to increase when the blades begin to stall. On a pitch regulated turbine the tower load is reduced at wind speed higher than rated wind speed ($\approx$ 11 m/s), since the blades pitch out of the wind and thereby reduce both the energy capture and the trust. At low wind speeds, the turbine experiences large yaw angle errors (Figure 10) with a mean yaw error on up to 25 deg and excursions up to 60 deg. The standard deviation is also high, indicating that there is a lot of yaw motion. The Gaia turbine has a free yaw system and therefor no active control of the yaw setting. Instead of a yaw control, the turbine is designed such that the aerodynamic forces will oriented the turbine correct in the wind. However, at low wind speeds the aerodynamic forces are low and therefore the turbine is less stable in yaw. The teeter excursions increase with wind speed and become relatively large for the higher wind speeds. The real teeter mechanisms have a teeter limit on 16 deg, so the largest teeter excursions will be limited by a stop mechanisms. Figure 11 shows the teeter angle for the simulation of normal power production at 17 m/s. It is only a few instances where the teeter angle exceeds the teeter limit (black line), not more than the teeter stop mechanisms can cope with.

Turbine Response to Platform Motion Together with the statistics for tower bottom bending moment figure 9 shows that the tower bottom bending moment contribution from tower top mass offset as function of static tower tilt (red line). The bending moment contribution is not zero at zero tower tilt, since the center of the gravity of the

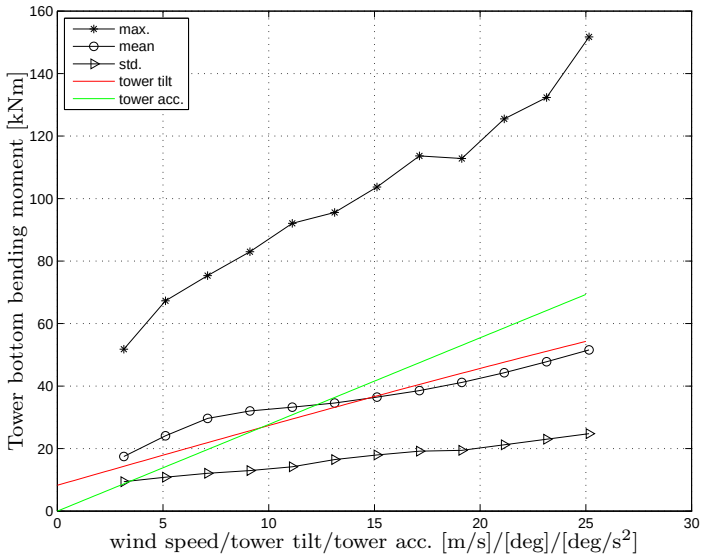

Figure 9. Statistics for tower bottom bending moment at normal operation. Red line shows the tower bottom bending moment caused by the offset of the center of gravity as a function of tower tilt angle. Green line shows the tower bottom bending moment caused by angular acceleration of the tower.

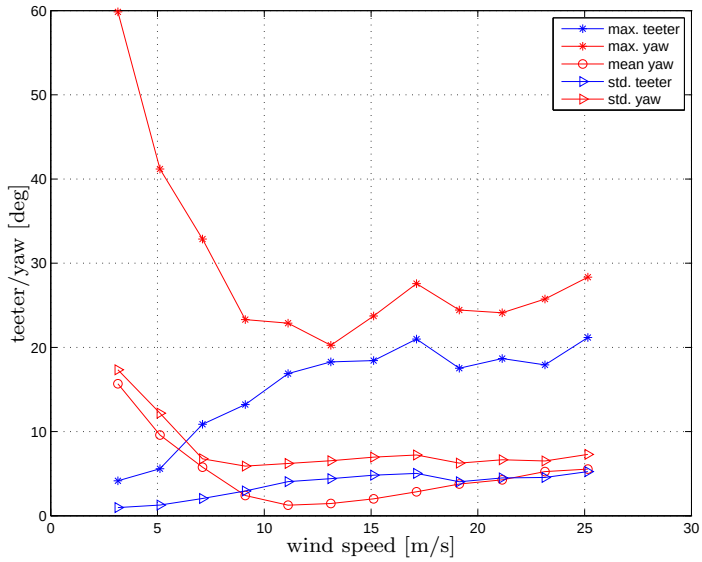

Figure 10. Statistics for teeter and yaw angle at normal operation.

tower top mass is not located on the tower top, but between the tower and the rotor (≈ 0.895 m from tower center).

For the Gaia turbine the contribution of bending moment at tilt angle values less than 5 deg is much smaller then the bending moment which occurs at normal operation, hence the tower tilt may not be a problem for the Gaia turbine. However, if a turbine is linearly upscaled the tower top mass increase proportional to R^3 (where R is the rotor radius) and aerodynamic trust increases proportional to R^2. Hence the relative effect on tower bottom bending moment causes by tower top mass combined with tower tilt increases with the turbine size. For MW size turbines, the tower bottom bending moment will be dominated by the effect of tower tilt combined with the tower top mass

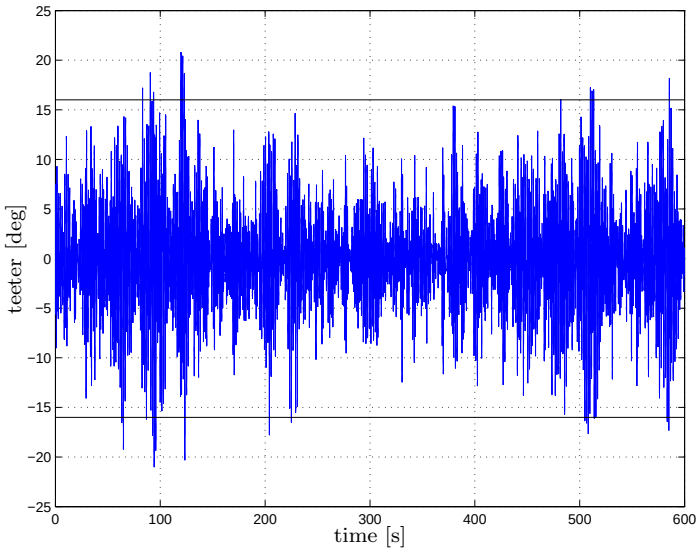

Figure 11. Teeter motion for time simulation at normal operation at 17 m/s

at only a few degrees of tilt.

Figure 9 shows that the tower bottom bending moment caused by the angular acceleration of the tower, corresponding to roll or pitch acceleration of the platform. The measurements show roll and pitch accelerations on up to 3 deg/s^2, so the bending moment contributions for inertia forces are also much smaller than the bending moment under normal operation. Again this effect increases for larger turbines because of the uneven scaling of tower top mass and aerodynamic trust, but the acceleration is expected to reduce if the platform and turbines are up-scaled, so the effect of up-scaling is unclear.

The platform motion is modeled in the aeroelastic simulations by placing two bearings in the tower bottom, such that the tower can tilt in longitudinal and lateral directions. The bearings are controlled by a PI controller tracking the measured motion of the platform. The controller applies a moment to the bearing, instead of prescribe the angle, to insure a smooth motion of the tower and to avoid convergence problems in the simulation. Figure 12 shows the measured and the simulated roll and pitch of the platform. The measurements are from 6:00 AM the 5th Jan 2009 where the significant wave height was $Hm0 = 0.96m$, one of the largest measured wave height in the measurement campaign. Figure 13 and 14 show the turbine's response to the platform motion at a mean wind speed of 5 m/s with a turbulent intensity of 0.225.

Figure 13 shows that the teeter motion exceeds the 16 deg limit only a few times, and that result is almost the same as the one found in the case with fixed turbine foundation (Figure 11). The yaw motion stays within acceptable limits and, most importantly, it doesn't rotate a full 360 deg. The longitudinal tower bottom bending moment increases slightly and that doesn't create any critical conditions. The lateral tower bottom bending moment increases a lot and become the dominating tower load. The results indicate that there will be a higher tower load on a turbine mounted floating foundation.

Effect of Turbines on the Platform Figure 15 shows the average work done by the controller on the turbine to realize the measured platform motion shown in figure 12. This work corresponds to the damping effect of the turbine on the platform motion.

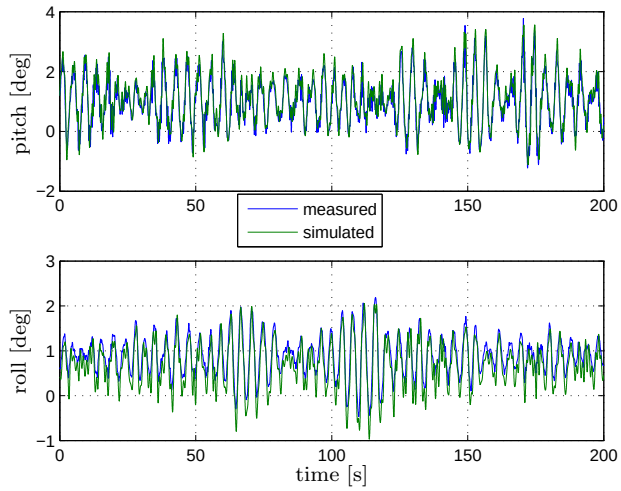

Figure 12. Measured and simulated platform pitch and roll at 6:00 AM 5th Jan 2009.

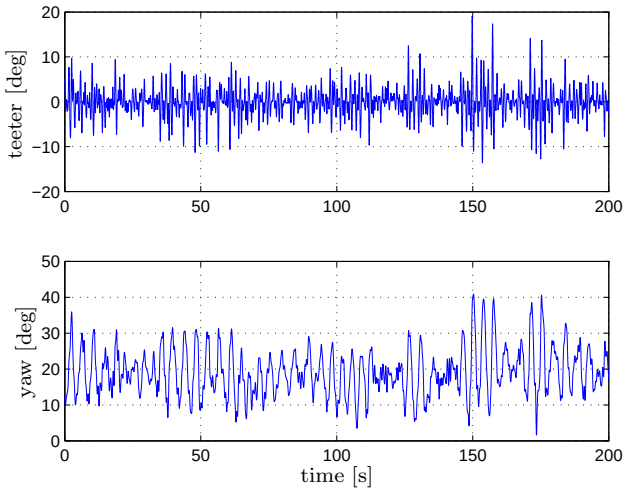

Figure 13. Teeter and yaw response to the platform motion shown in Figure 12

It is seen that the turbine adds most damping in the lateral direction (platform roll), which is unexpected, since normally turbines are low aerodynamically damped in the lateral direction. The reason to that is the free yaw, which changes the characteristic behavior of the turbine. The damping for a similar turbine with a fixed yaw is also shown in figure 15. The damping for the fixed yaw turbine is seen to be completely different from the one with free yaw. If a pitch regulated turbine is used, the pitch controller can be used actively to change the damping of the platform.

4.4 Summary

This chapter presents the results of an application of combining wave and wind energy technologies together. The basis of the application is a floating power plant called Poseidon which consists of offshore wind turbines that are mounted on a wave energy plant. Tests related to wave energy part have been realized at the sea and a comprehensive

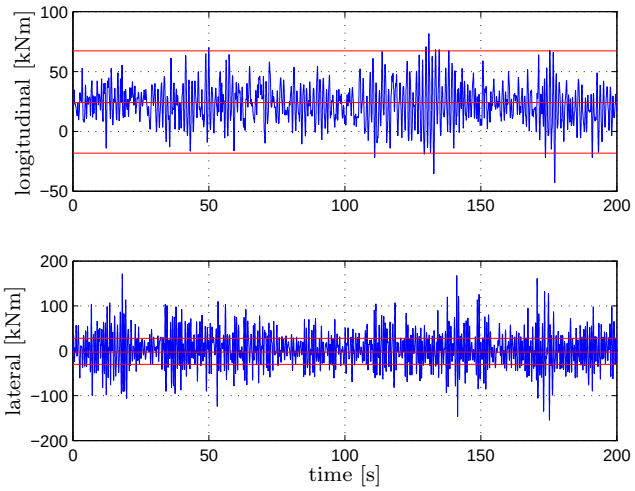

Figure 14. Tower bottom bending moment responses to the platform motion shown in Figure 12. The red lines indicates the minimum, mean and maximum for the simulations without platform motion.

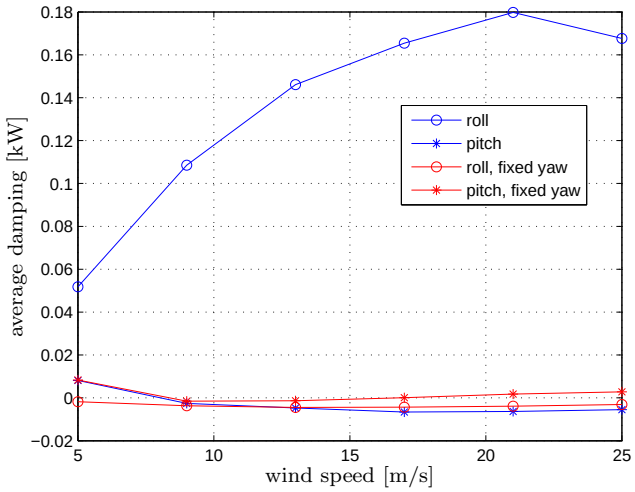

Figure 15. Average work done to make the tower follow the platform motion.

measurement campaign has been carried out to measure the platform motion together with the environmental conditions (wave, current and wind characteristics). The measurements formed the basis for the aeroelastic simulations of a wind turbine mounted on the platform. The turbine, which will be mounted on the Poseidon platform, is modeled in HAWC2 (Risø's aeroelastic code developed for modeling wind turbines) and the measured platform motion is imposed at the tower bottom. The aeroelastic simulations indicate that wind turbines can be mounted on the floating wave energy platform, but the tower bottom bending moment has increased, and extra considerations has to be taken in turbine tower construction.

The specific turbine is found to damp the roll motion of the platform, however other turbine concepts will give different damping effect on the floating platform.

5 Results from second measurement campaign

By RisøDTU

This chapter deals with the measurement from the second test period, where the platform was tested at sea with turbines.

5.1 Experimental setup

The platform has been heavy instrumented, in order to record turbine loads, platform motion, and wind and wave characteristics. The maximum wave height, significant wave height, wave period, zero crossing period, wave direction, current speed and direction are measured by an Acoustic Doppler Current Profiler (ADCP). Full (direction-frequency) wave spectra were also recorded. There have been some problems with this ADCP resulting in periods without wave data. The maximum wave height data from an ADCP is often of poor quality and it will not be used here. The wave and current conditions are stored as mean values, sampled every 5 minutes. The wind speed and direction are measured with a sonic placed on a 12 m mast (hub height) on the platform and sampled at 35 Hz. The platform direction is measured by two GPS, one on each side of the platform and sampled one time each minute. The platform roll and pitch is measured by two inclinometers and sampled at 35 Hz. The inclinometers have a typical time constant better than 0.3 seconds. The platform is also equipped with one three-axis accelerometer at each turbine foundation sampled at 35 Hz. For the three wind turbines the following signals are measured: tower top and bottom bending moment in 2 directions, rotor shaft torque, rotor shaft bending, moment in two directions, blade root flap and edge wise bending moment, rotor blade position, teeter and yaw position. All the turbine signals are sampled at 35 Hz. The demonstration platform has been at sea for approximately four months. Accounting for periods with signal outages and special test campaigns a total of 6799 10 minutes time series are available for analysis.

5.2 Wind and wave conditions

This section deals with the wind and wave conditions during the test period. Figure 16 shows the location of the test platform in the confined Danish waters north of the island of Lolland. As for most wave energy conversions systems the Poseidon wave conversions concepts need to be scaled to fit the specific wave climate, and the wave climate in these confined waters fit the scaled demonstration platforms size. Figure 17 shows the wind and wave measurements during the test period. The platform is located just west of Vindeby wind turbine park, and the wake from this is the reason for the low wind speeds observed from east. The wind and wave is seen not to coincide, mainly because of the wind shadow from the Vindeby park and the wave shadow from the shore of Lolland. The difference in wind and wave conditions allow for analyzing the platform in conditions corresponding to both, high wind low waves and vice versa.

5.3 Platform Motion

In this section the platforms motion is analyzed. The platform motions will be described in the ship motions terms shown on figure 18(a). Figure 18(b) shows the 10 min mean values of the platform pitch and roll for the test period. The platform pitch and roll ex-

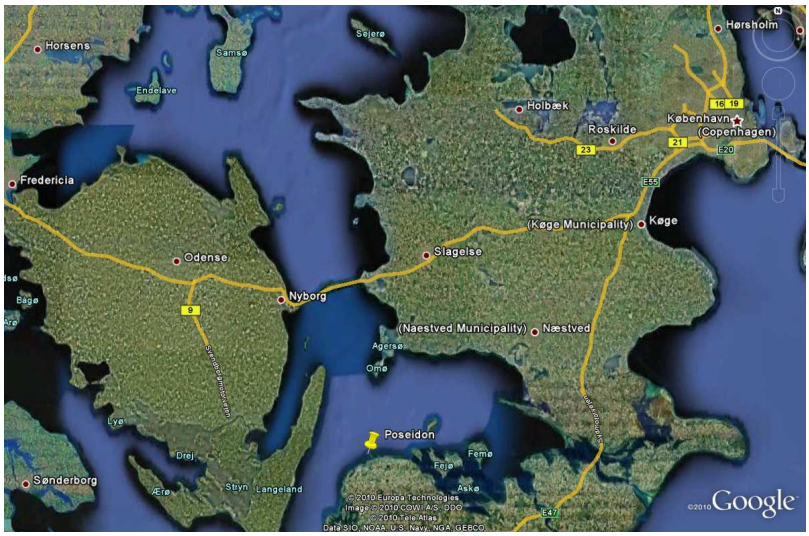

Figure 16. Location of the Poseidon demonstration platform just north of Lolland.

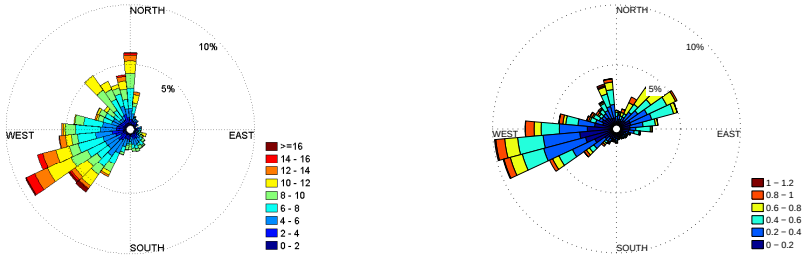

(a) (b)

Figure 17. (a) Wind and (b) wave rose for the Poseidon site, measured during the measurement campaign.

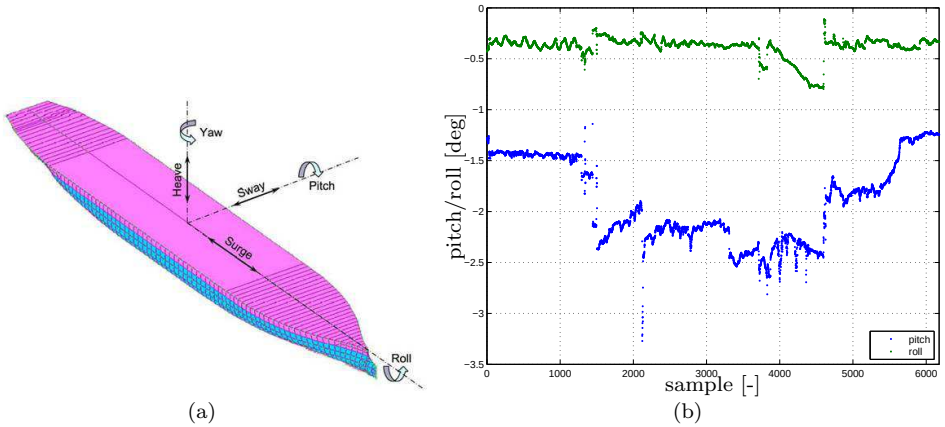

(a) (b)

Figure 18. a) Definition of platform motion. The sign on pitch and roll are opposite as shown, the surge is positive when the platform is moved backwards, sway is positive when the platform is moved towards starboard and heave is positive when the platform is moved downwards. b) 10 minutes mean platform tilt and roll during the test period.

cursions are very important parameters for floating turbine foundations. Platform pitch and tilt will give the turbine towers a tilt relative to the original vertical orientation. The turbine tower tilt, together with the tower top mass, can creates a considerable contribution to the tower bottom bending moments. The mean platform pitch is seen to be kept within -3.5 to -1 deg, and the stepwise character of the pitch shows that it is mainly determined by how the platform is ballast and not by the external effects from waves and wind. The mean platform pitch excursions will easily be reduced if keeping the pitch constant is higher prioritized in the control of the platform's ballast system. The mean platform roll is seen to be kept within -1 to 0 deg. Figure 19(a) shows the absolute value of minimum and maximum pitch and roll angles for each 10 minutes time series relative to the mean of the respectively time series. Generally the

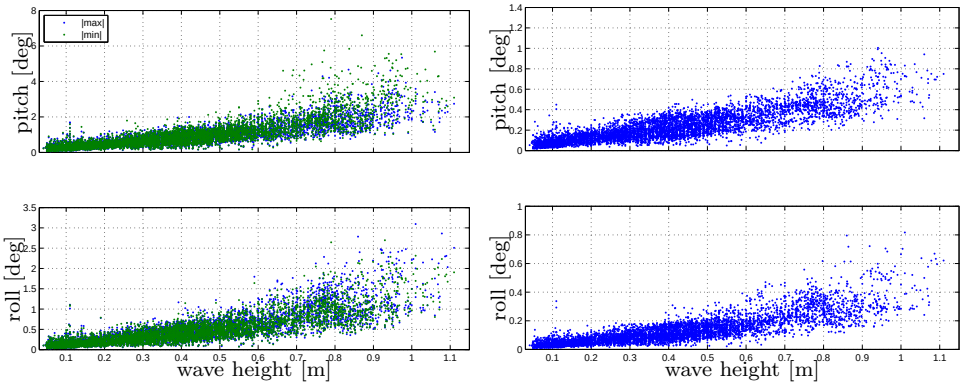

Figure 19. platform amplitude (a) and standard deviation (b) of the platform versus wave hight.

roll motion is seen to be smaller compared to the pitch motion. Since the platform is wider than it is long it will generally be more stable in roll than pitch. Furthermore, because the platform is aligned with the waves, the wave loading on pitch is higher. The seven highest pitch values are from the same day, the 15th of September 2010. The reason for these high pitch excursions on that particular day is not clarified yet, but it is a major point for further analysis.

Figure 20 shows the standard deviation as function of significant wave height for two set of cases, one where all turbines are stopped and one where at least two turbines are running. A second order polynomial fit to the two data sets is also shown. The fitted trend lines indicate that for large waves there are less pitch motions when the turbines are running than when they are stopped. This shows that the large aerodynamic damping for longitudinal rotor motion damp the overall platform motion. For small waves the platform activity is largest when the turbines are running, this is because in this cases, with small waves, the main load input on the platform is the turbines. The turbines effect on roll is small for large waves, corresponding to the low aerodynamic damping of lateral rotor motion.

Figure 21 shows the power spectrum for platform pitch and roll. Four different power spectrums are shown for the pitch and roll, dividing the operation conditions into significant wave height smaller than 0.07 m and larger than 0.7 m, with and without the turbines running. The platforms rigid surge, heave, roll and pitch frequencies has been computed by the comprehensive radiation-diffraction program WAMSIM[5, 6] to be 0.017, 0.098, 0.146 and 0.203 Hz, respectively. The peak wave frequency is around 0.3 Hz. The broad band wave excitation of the rigid platform motion is causing the large energy in the 0.15 to 0.4 Hz region. The peaks at 1.2 and 1.5 Hz are structural platform frequencies. The turbines are seen to introduce a large peak at ≈1.86 Hz and

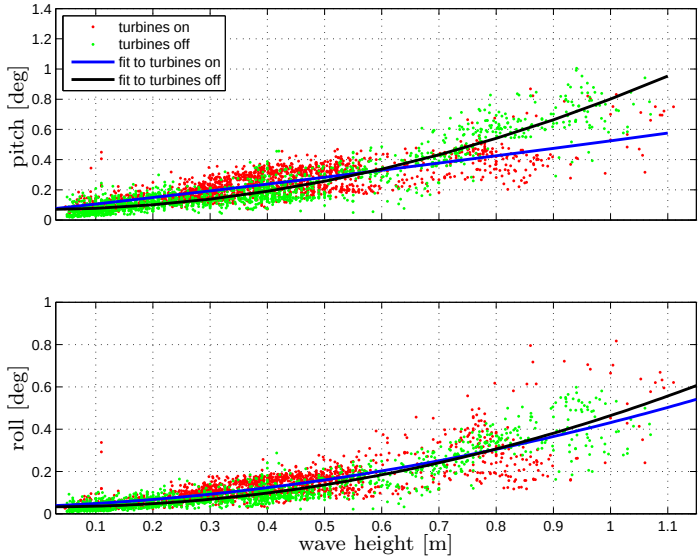

Figure 20. Standard deviation of platform motion when all turbines are stopped and when at least two of them are running, respectively, and a fit to the two data sets.

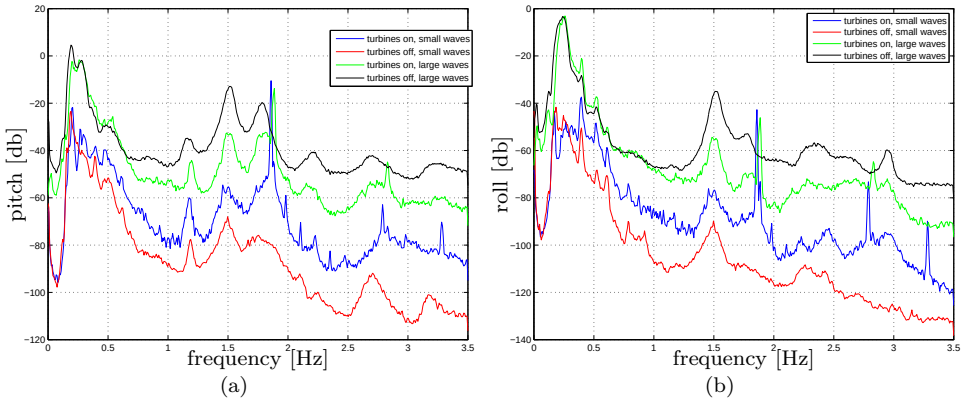

Figure 21. Platform power spectrum for pitch (a) and roll (b) at different operational conditions.

higher harmonics. This corresponds to two times the rotors rotation frequency, which is well known to be important for two bladed turbines. For the case with small waves the main load input to the platform is the turbines, so it is natural that the power spectrum shows higher energy levels at most frequencies. For the the large waves cases the low frequency load spectrum is seen to be the same with and without the turbines running. At these frequencies the platform motion is dominated by wave loads and the motion is to slow to affect the rotor aerodynamic, and thereby adding damping. For the higher frequencies the general energy level is lower when the turbines are running, indicating that the turbines add damping to these frequencies. The indications from this frequency plot corresponds well to the discussion based on Figure 20.

In conclusion the platform is seen to be very stable in the water with only small excursions from the mean position. The turbine is found to have a stabilizing effect on pitch for large waves while they slightly increase the platform motion in both roll and pitch for small waves.

5.4 Wind turbine loads

The floating and thereby dynamic foundation gives the turbines a new operation environment which changes the loading on the turbines. Some new issues arising from this operation environment will be analyzed in this section, using the measurements from the test platform.

As mentioned above a major concern for floating turbine concepts are pitch and roll stability of the supporting platform. The tower tilt caused by such motion can give a considerable contribution to the tower bottom bending moment, changing the tower design criteria.

To analysis the effect of tower tilt Figure 22(a) shows the platform pitch angle from a time series with a mean wind speed on 1.6 m/s but relative large platform motions. The low wind speed minimizes the effect of aerodynamic loading on the tower bottom bending moments. The figure also shows a simple harmonic function fitted to the measurements, this function is used to estimate the effect of platform pitch on the tower bottom bending moment. Figure 22(b) shows the longitudinal tower bottom bending

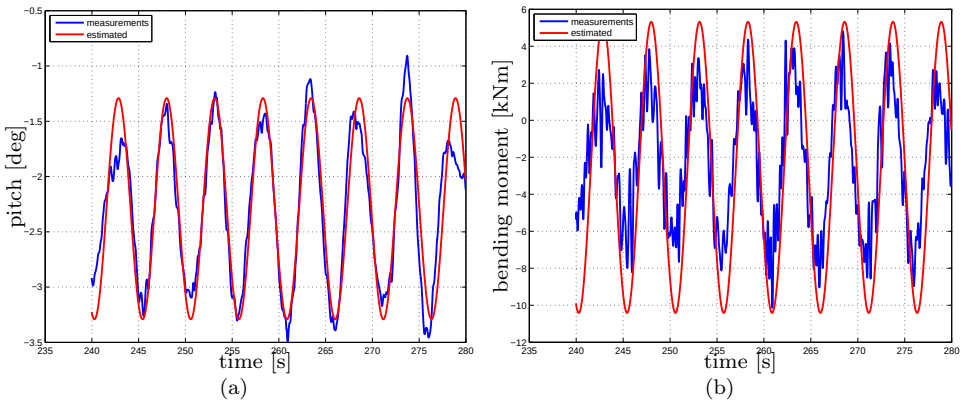

Figure 22. a) Measured platform pitch angle and a simple harmonic function fit b) Measured bending moment together with an estimated of the bending moment caused by static and dynamic tower tilt. The estimated bending moment is based on the simple harmonic fit to the pitch motion (Figure 22(a)).

moment for the same time period. An estimated bending moment based on the simple harmonic function fitted to the pitch motion, tower mass and tower top mass is also shown. The estimated bending moment is seen to fit the measured fairly well. The platform motions has two contributions to the tower bending moment; the quasi static effect of tower and tower top mass overhang and the dynamic effect of accelerating the tower and tower top mass. In this case, with relative large pitch oscillations, the dynamic contribution from acceleration is approximately twice the contribution from the quasi static effect of overhang.

To compare these tower load contribution from platform motion to the operation loads Figure 23 shows the 10 minuets mean, maximum and minimum values for the longitudinal tower bottom bending moment with the turbine running. The tower bottom bending moment caused by tower tilt is oscillates with around 14 kNm peak to peak, which is seen to be small compared to the bending moments during operation (Figure 23).

The issue concerning tower tilt is relative larger for large turbines than for the small turbines used in this project. This is because the aerodynamic trust scale by approxi-

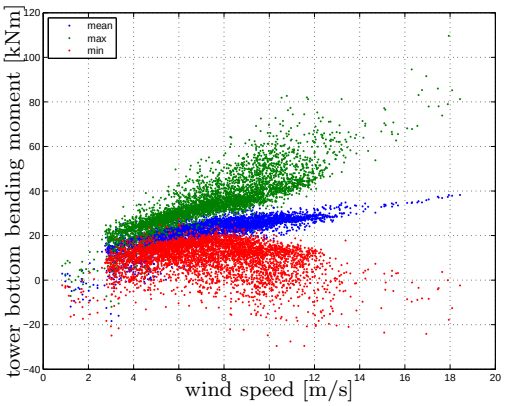

Figure 23. 10 minutes mean, maximum and minimum values for the longitudinal tower bottom bending moment with the turbine running.

mately R^2 while the tower and tower top mass scale by approximately R^3, where R is the rotor radius.

To analysis the extra fatigue on the turbine tower caused by the platform motion figure 24(a) shows the standard deviation for longitudinal tower bottom bending moment versus wind speed. The standard deviation is not a direct fatigue measure, but it is a good indicator. The results are split into two cases; one with a standard deviation on the platform pitch motion less than 0.3 deg and one where it is larger than 0.4 deg, denoted as small and large platform pitch motion, respectively. Because the platform motion

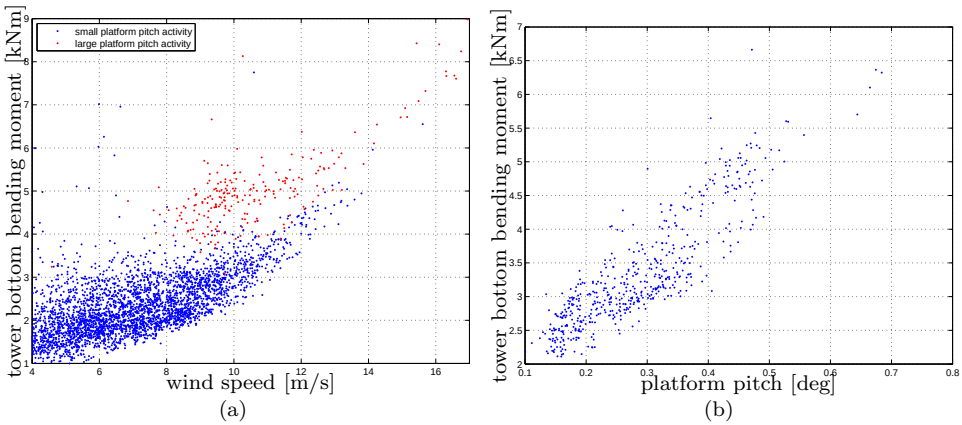

Figure 24. a) 10 minutes standard deviation for the longitudinal tower bottom bending moment with the turbine running versus wind speed. b) 10 minutes standard deviation for the longitudinal tower bottom bending moment with the turbine running for wind speed between 9 and 10 m/s versus standard deviation of platform pitch motion.

depends on the waves, which again depends on the wind, there is not many occurrences with the same wind speeds but different platform activity, anyway for the 8 to 14 m/s region there are some overlap. It is clearly seen that the extra platform activity adds to the tower fatigue. Figure 24(b) shows the relation between standard deviation of longitudinal tower bottom bending and standard deviation of platform pitch for wind speeds between 9 and 10 m/s. The results indicate that the tower fatigue is linear increasing with the platform activity. Figure 25 shows the standard deviation of the edgewise, and flapwise blade root bending moment for wind speeds between 9 and 10 m/s versus standard deviation of the platform pitch. It is seen that the platform motion does not affect the blade loads.

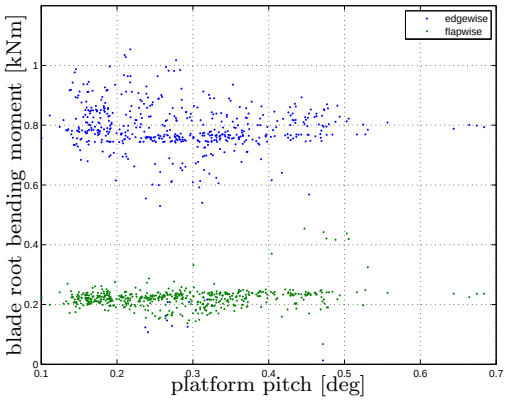

Figure 25. Standard deviation of blade root bending moments for wind speeds between 9 and 10 m/s versus standard deviation of platform pitch.

5.5 Summary

This paper present results from the second test phase, where the platform was tested with turbines. The wind and wave climate of the test site are presented and the corresponding platform motion is analyzed and discussed. It is found that the platform excursions are kept within an acceptable range for supporting classical wind turbines. Furthermore it is found that the turbines have a stabilizing effect on the platform at large waves. An analysis of the turbine load measurements shows that the turbine tower loads increase with increased platform motion, as expected, and that the blade loads one the other hand are not affected by the platform motion.

6 Structural and hydrodynamic model of a moored and ballasted floating mono-pile for implementation in FLEX5

By DONG

6.1 Introduction

In this note the structural and hydrodynamic equation of motion for a moored and ballasted floating mono-pile is derived. In figure 26 below, an elevation plan of the plant is shown. The following points and levels are of interest in respect of the dynamics of

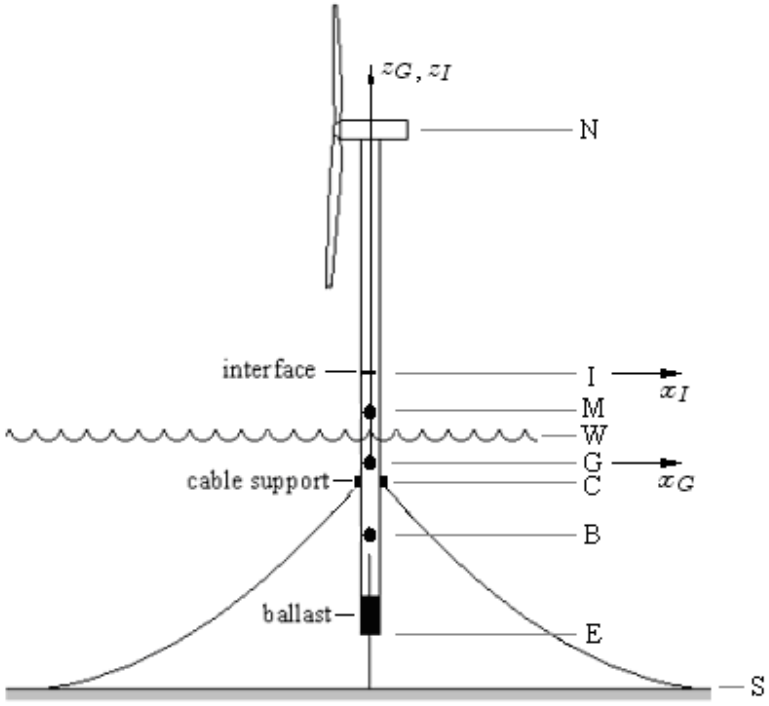

Figure 26. Elevation plan for moored and ballasted floating monopole.

the floating wind turbine - these are

N	nacelle centre
I	the interface point defining the separation between the tower and the mono-pile (this has practical and not theoretical implication)
M	the meta-centre point, which is the natural point of rotation for a free floating (non-moored and non-dynamical loaded) structure
W	water surface level
G	the structural centre of gravity
B	the buoyancy centre, i.e. the centre of gravity for the displaced water
E	the mono-pile bottom
S	sea bed level

The following notation is used for the internal dimensions,l_{ij}, which represents the

length/distance from point/level i to point/level j, e.g. l_{EI} is the length from point E to point I, i.e. the full length of the mono-pile.

Two coordinate systems are considered - one at point I,(z_I, y_I, z_I), and one in point G,(x_G, y_G, z_G).

In the G-system, the motion of the mono-pile is described by the following 6 DOFs:

q_{x_G}	fore-aft displacement, [m]
q_{y_G}	side-side displacement, [m]
q_{z_G}	negative heave, [m]
θ_{x_G}	side-side roll, [rad]
θ_{y_G}	fore-aft roll, [rad]
θ_{z_G}	yaw, [rad]

Above DOFs are collected in the vector,$\mathbf{q}_G$. In figure 27 the components of $\mathbf{q}_G$ are shown

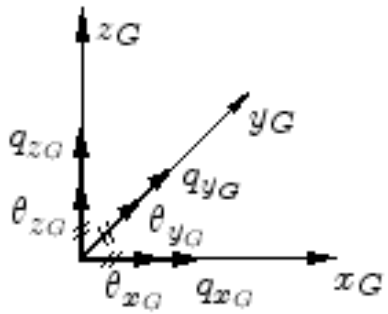

Figure 27. orientation of the components of $\mathbf{q}_G$ *in G.system*

And in the I-system by corresponding DOFs, $(q_{x_I}, q_{y_I}, q_{z_I}, \theta_{x_I}, \theta_{y_I}, \theta_{z_I})$ collected in the vector,$\mathbf{q}_I$.

Additional, the following mass per unit length apply for the mono-pile

$\mu_s(z)$	mass per unit length of mono-pile structure, (ballast included) [kg/m]
$\mu_w(z)$	mass per unit length of displaced water, [kg/m]

The total structural mass of the wind turbine, tower and mono-pile is

$$m_T = m_N + \int_{-l_{EG}}^{l_{GN}} \mu_s(z_G)\, dz_G \tag{1}$$

m_N nacelle and rotor mass, [kg]

The total displaced water volume,V_w, becomes

$$V_w = \frac{m_T}{\rho_w} = \frac{\pi}{4} \int_{-l_{EG}}^{l_{GW}} D^2(z_G)\, dz_G \tag{2}$$

ρ_w is the water density, [kg/m^3]
$D(z)$ is the mono-pile outer diameter, [m]

The length of the submersible part of the mono-pile,l_b, must implicit be found from (1) and (2).

*E*xample 1.a

---

if $D(z_G) = c\text{onst.} = D_0 \Rightarrow$

$$V_w = \frac{\pi}{4} D_0^2 \, l_{EW} \tag{3}$$

if additional $\mu_s(z) = \mu_{s,0} \Rightarrow$

$$m_T = m_N + \mu_{s,0} \, l_{EI} \tag{4}$$

Using (2), (3) and (4)

$$l_b = \frac{4}{D_0^2 \, \pi \, \rho_w} \left(m_N + \mu_{s,0} \, l \right) \tag{5}$$

if $m_N = 0$ and $D_0 = lm$, $t = 0.01$ m (tower and pile thickness) $\Rightarrow$

$\mu_{s,0} = \frac{\pi}{4} \left(1^2 - (1 - 2 \cdot 0.01)^2 \right) \cdot \rho_s = 244$ kg/m, (ρ_s assumed to be 7850 kg/m^3)

$l_{EW} + l_{WN} = 100$ m, $\rho_w = 1100$ kg/m^3 $\Rightarrow$ $\mu_{s,0} \cdot l = 24400$ kg and $\mu_w = 864$ kg/m (mass per unit length of displaced water in mono-pile) $\Rightarrow$

$l_{EW} = 28.24$ m

Hence weight of displaced water is $m_w = \frac{\pi}{4} \cdot 1^2 \cdot 28.24 \cdot 1100 = 24398$kg which is the same as the total structural weight of 24400kg

---

6.2 Loads acting on the mono-pile

All loads, that is elastic, damping and inertial loads origin from the water, the air and the structure will be characterised and prioritised in the following. In order to ease the EOM formulation the present approach is only to include uncoupled loading effects on the mono-pile.

a. Sectional forces from the wind turbine at the interface point:
$(F_{x_I}(t), F_{y_I}(t), F_{z_I}(t), M_{x_I}(t), M_{y_I}(t), M_{z_I}(t))$

b. Horizontal wind load on the above MSL part of the mono-pile, fore-aft: $p^{(x)}_{wind}(z_G, t, \dot{q}_{x_G}, \dot{\theta}_{y_G})$
and side-side: $p^{(y)}_{wind}(z_G, t, \dot{q}_{y_G}, \dot{\theta}_{x_G})$

c. Horizontal[2] wave load on the below MSL part of the mono-pile, fore-aft: $p^{(x)}_{wave}(z_G, t, \dot{q}_{x_G}, \dot{\theta}_{y_G}, \ddot{q}_{x_G}, \ddot{\theta}_{y_G})$
and side-side: $p^{(y)}_{wave}(z_G, t, \dot{q}_{y_G}, \dot{\theta}_{x_G}, \ddot{q}_{y_G}, \ddot{\theta}_{x_G})$

d. Hydrostatic restoring moment of fore-aft roll motion: $M^{(y)}_{hs}(\theta_{y_G})$ and side-side ditto $M^{(x)}_{hs}(\theta_{x_G})$

[2]For the time being, vertical wave loading and current are ignored

e. Hydrodynamic damping force due to heave velocity from drag on the mono-pile bottom and mono-pile surface friction: $F_{hd}^{(z)}(\dot{q}_{z_G})$

f. Heave displacement force from buoyancy: $F_{hs}^{(z)}(q_{z_G})$

g. Heave displacement force from vertical mooring cable reactions: $F_{cs}^{(z)}(q_{z_G})$

h. Horizontal mooring cable reaction forces due to fore-aft rolling and displacement: $F_{cs}^{(x)}(q_{x_G}, \theta_{y_G})$ and side-side ditto: $F_{cs}^{(y)}(q_{y_G}, \theta_{x_G})$

i. Torsional reaction moment from mooring cable reaction forces due to mono-pile torsion: $M_{ct}^{(z)}(\theta_{z_G})$

The forces described in a. - c. are explicit time dependent and termed external loads and placed on the right-hand side in the EOM. The forces described in d. - i. can be considered (by free choice) as contribution to the system stiffness and damping properties and placed on the left-hand side of the EOM.

In the following, each of the above stated loads will be described in more detail and the associated contributions to the system properties, that is stiffness and damping will be derived.

a. Sectional forces from the wind turbine tower at the interface point
The cross sectional forces in the intersection point, I, $(F_{x_I}(t), F_{y_I}(t), F_{z_I}(t), M_{x_I}(t), M_{y_I}(t), M_{z_I}(t))$, originate from dynamic loads on the wind turbine rotor and tower. As mentioned they will be considered as external loads on the right hand side of the EOM.

b. Horizontal wind load on the above MSL part of the mono-pile
The horizontal wind load in fore-aft direction is given as

$$p_{wind}^{(x)}(z_G,t) = 1/2\ \rho_{air}\ D(z_G)\ C_{D,wind}\ |U_{wind}(z_G) + u_{wind}^{(x)}(z_G,t) - \dot{u}_{x_G}(z_G,t)| \cdot \left(U_{wind}(z_G) + u_{wind}^{(x)}(z_G,t) - \dot{u}_{x_G}(z_G,t)\right) \tag{6}$$

and in the side-side direction

$$p_{wind}^{(y)}(z_G,t) = 1/2\ \rho_{air}\ D(z_G)\ C_{D,wind}\ |u_{wind}^{(y)}(z_G,t) - \dot{u}_{y_G}(z_G,t)| \cdot \left(u_{wind}^{(y)}(z_G,t) - \dot{u}_{y_G}(z_G,t)\right) \tag{7}$$

ρ_{air}	density of air
$C_{D,wind}$	aerodynamic drag coefficient of mono-pile
$D(z_G)$	outer diameter of mono-pile
$U_{wind}(z_G)$	mean wind speed in -direction (assumed to be the mean wind direction)
$u_{wind}^{(x)}(z_G,t)$	wind turbulence in -direction
$u_{wind}^{(y)}(z_G,t)$	wind turbulence in -direction

Further $\dot{u}_{x_G}(z_G,t) = \dot{q}_{x_G}(t) + z_G \cdot \dot{\theta}_{y_G}(t)$ is the horizontal mono-pile displacement velocity in section z in fore-aft, x, directions and for the side-side, y, direction $\dot{u}_{y_G}(z_G,t) = \dot{q}_{y_G}(t) - z_G \cdot \dot{\theta}_{x_G}(t)$.

c. Horizontal wave load on the below MSL part of the mono-pile
The horizontal wave load in the fore-aft direction is given by the Morison equation as

$$p_{wave}^{(x)}(z_G,t) = 1/2\ \rho_{water}\ C_{D,wave}\ D(z_G)\ |v_{wave}^{(x)}(z_G,t) - \dot{u}_{x_G}(z_G,t)|\ \left(v_{wave}^{(x)}(z_G,t) - \dot{u}_{x_G}(z_G,t)\right) + \pi/4\ \rho_{water}\ D^2(z)\ \left(\dot{v}_{wave}^{(x)}(z_G,t) + C_{a,wave}\ (\dot{v}_{wave}^{(x)}(z_G,t) - \ddot{u}_{x_G}(z_G,t))\right)$$

(8)

and in the side-side direction

$$p^{(y)}_{wave}(z_G,t) = 1/2\ \rho_{water}\ C_{D,wave}\ D(z_G)\ |v^{(y)}_{wave}(z_G,t) - \dot{u}_{y_G}(z_G,t)|\ \left(v^{(y)}_{wave}(z_G,t) - \dot{u}_{y_G}(z_G,t)\right) + \pi/4\ \rho_{water}\ D^2(z_G)\ \left(\dot{v}^{(y)}_{wave}(z_G,t) + C_{a,wave}\ (\dot{v}^{(y)}_{wave}(z_G,t) - \ddot{u}_{y_G}(z_G,t))\right) \tag{9}$$

$\rho_{water} = 1025$ kg/m^3 is the density of sea water
$C_{a,wave}$ is the added hydrodynamic mass (approx 1, but depends on the Reynolds and Keulegan Carpenter numbers and the wave number)

Including relative velocities in the wave loading the hydrodynamic damping has automatic been accounted for. To include the hydrodynamic damping on the left hand side of the EOM requires a linearization of Morison's equation which will not be done here.

d. Hydrostatic restoring moment of fore-aft roll motion
Taking moment equilibrium in point G in below figure 28 the hydrostatic moment, $M^{(y)}_{hs}(\theta_{y_G})$, becomes

$$M^{(y)}_{hs}(\theta_{x_G}) = -V_w\ \gamma_w\ l_{GM}\ \theta_{y_G} \tag{10}$$

$\gamma_w = \rho_w\ g$ is the specific weight of sea water g is acceleration of gravity, [m/s^2] and

The following relation exist between l_{BG} and l_{GM}:

$$l_{GM} = \frac{I_w}{V_w} - l_{BG} \tag{11}$$

I_w moment of inertia at water line, i.e. $I_w = \dfrac{\pi}{64}\ D^4(z_G = l_{GW})$

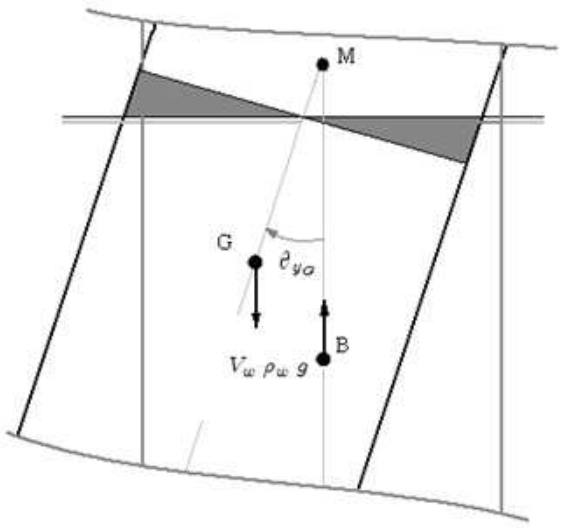

Figure 28. Hydrostatic forces and moments due to fore-aft roll

Inserting (11) into (11) gives

$$M^{(y)}_{hs} = -\gamma_w\ \theta_{y_G}\ \ (I_w - l_{BG}\ V_w) = -K^{(y)}_{hs}\ \theta_{y_G} \tag{12}$$

In which $K^{(y)}_{hs}$ is the hydrostatic stiffness due to fore-aft roll.

Since the mono-pile have circular section the hydrostatic stiffness in side-side roll, $K_{hs}^{(x)}$, is equal to $K_{hs}^{(y)}$.

Note that there are no hydrostatic loads originating from fore-aft or side-side displacements, i.e. from (q_{x_G}, q_{y_G}).

e. Hydrodynamic damping force due to heave velocity from drag on the mono-pile bottom

The drag force on the mono-pile bottom due to heave velocity, $\dot{q}_{z_G}$, is not intuitively derived. However, based on [11][3], the drag force may be found from

$$F_{hd}^{(z)} = -C_D^{(z)} \cdot \dot{q}_{z_G} \tag{13}$$

$$C_D^{(z)} = 2\,\zeta\,\omega_{z_G}\,\left(m_T + m_a^{(z)}\right) \tag{14}$$

m_T	can be found from (1)
$\zeta =$	0.2
ω_{z_G}	= cyclic/angular frequency of heave mode
$m_a^{(z)}$	= hydrodynamic added mass in heave mode found from

$$m_a^{(z)} = \rho_w C_m\, 2\pi/3\, D^3(z_G = l_{BW}) \tag{15}$$

Then the hydrodynamic damping factor is given by

$$C_{hd}^{(z)} = -C_D^{(z)} \tag{16}$$

The problem here is the implicit relation between w_{z_G} and $\zeta_{hd}^{(z)}$ though the associated eigen-value problem with damping included valid for the heave mode. A more simple approach, see [12], is, in spit of physical support, to apply Morisons drag equation

$$F_{hd}^{(z)} = -\frac{1}{2}\,\rho_w\,\dot{q}_{z_G}\,|\dot{q}_{z_G}|\,\frac{\pi}{4}D^2(z_G = l_{BW} - l_{GW})\,C_D^{(z)} \tag{17}$$

Where $C_D^{(z)} = 20$ and $D(z_G = l_{BW} - l_{GW})$ is the mono-pile bottom diameter.

f. Heave displacement force from buoyancy

An increase in the water surface level, δz_G, will also change the location of buoyancy center and hence the buoyancy force, $F_B^{(z)}$. In figure 29 this is illustrated and corresponding geometric measures are shown.

Buoyancy force in z-direction for water surface level 1:

$$F_{B1}^{(z)} = \gamma_w \cdot \int_{l_{GW1}-l_{B1W}}^{l_{GW1}} D(z_G)\,dz_G \tag{18}$$

And for water surface level 2:

$$F_{B2}^{(z)} = \gamma_w \cdot \int_{l_{GW2}-l_{B2W}}^{l_{GW2}} D(z_G)\,dz_G \tag{19}$$

Subtracting (18) from (19) gives

$$\delta F_B^{(z)} = F_{B2}^{(z)} - F_{B1}^{(z)} = \gamma_w \cdot \int_{l_{GW1}}^{l_{GW1}+\delta z_G} D(z_G)\,dz_G \tag{20}$$

[3] In which the original references can be found

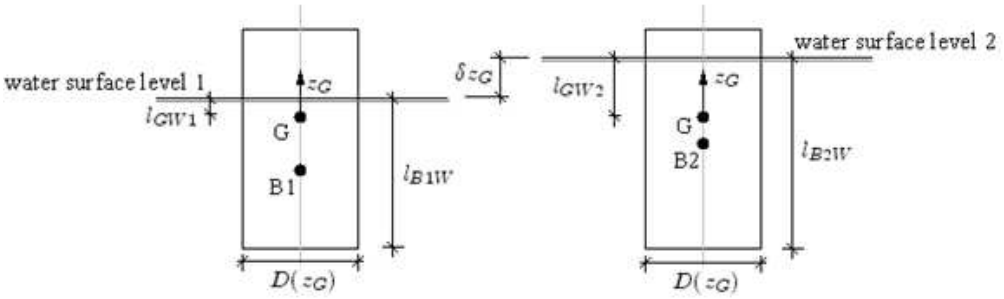

Figure 29. Illustration of change of buoyancy center due to an increase in the water surface level

From (20), the heave stiffness due to buoyancy, $K_B^{(z)}$, can be found to be

$$K_B^{(z)} = \frac{\delta F_B^{(z)}}{\delta z_G} = \frac{\gamma_w}{\delta z_G} \cdot \int_{l_{GW}}^{l_{GW}+\delta z_G} D(z_G)\, dz_G \tag{21}$$

Assuming $D(z_G) = \text{const} = D(z_G = l_{GW0})$ over the range $z_G \in [l_{GW};\ l_{GW} + \delta z_G]$ note[4] , where l_{GW0} is the z_G axis value for the water surface level[5] - then the buoyancy heave stiffness, $K_B^{(z)}$, becomes

$$K_B^{(z)} = \gamma_w \cdot D(z_G = l_{GW0}) \tag{22}$$

The stiffness given by (22) and the assumption behind it will be used in the formulation of the EOM.

g. Heave displacement force from vertical mooring cable reactions
Generally for the stiffness of the mooring cable is based on the assumption that the bending stiffness of the cable is insignificant (assumed zero) and that at the sea bed is that the cable lies flat on the sea bed prior to the support point/anchor. Additional the cable is assumed infinite stiff in axial tension thus the stiffness of the cable at the support point on the mono-pile is solely given by the gravity of the cable. These assumptions makes the cable follows a catenary[6] line.

In appendix 6.11, the derivation of the linearized vertical cable stiffness, $K_c^{(z)}$, can be found.

h. Horizontal mooring cable reaction forces due to fore-aft rolling and displacement
The same general assumptions as given for the vertical cable stiffness also apply for the horizontal mooring cable stiffness and the derivation of $K_c^{(x)}$ (fore-aft stiffness) and $K_c^{(y)}$ (side-side stiffness) can also be found in appendix 6.11.

i. Torsional reaction moment from mooring cable reaction forces due to mono-pile torsion
In figure 30 the mono-pile section at the cable support points is shown. The pre-tensioned cable force, F_c, due to buoyancy and cable gravity is not assumed to increase due to the tortional rotation of $\delta\theta_{z_G}$, since the cable length is much longer than the cable elongation due to the small torsional rotation. Additional, the direction of the cable force is not assumed to chance. The restoring force, F_t, tangential to perimeter of

[4]Note δz_G is not to be considered as a small value - but have a size corresponding to e.g. tide level and/or wave height applied in calculations/simulations

[5]z_{GW0} is assumed valid for a static load equilibrium state including all loads, that is gravity from turbine mono-pile and mooring cables and buoyancy.

[6]The word *catenary* is derived from the Latin word catena, which means chain

the mono-pile section thus become $F_t = sin(\delta\theta_{z_G})\ F_c \simeq \delta\theta_{z_G}\ F_c$. With three mooring cables the restoring torsion moment, M_t, thus becomes

$$M_t = 3\ F_t\ \frac{D}{2} \tag{23}$$

and the torsional stiffness, K_{ct}, becomes

$$K_{ct} = 3\ F_c\ \frac{D}{2} \tag{24}$$

so the cable pre-tensioning force, F_c, must be known prior to determine the torsion stiffness.

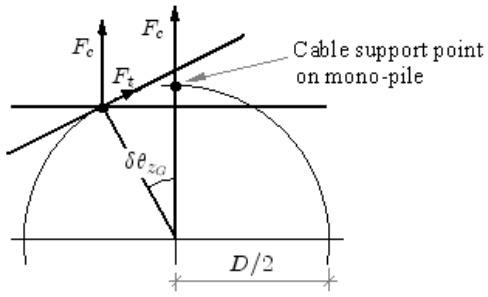

Figure 30. Induced cable force, F_T, from torsional rotation, $\delta\theta$, of mono-pile

6.3 Equation of motion (EOM)

The equations of motion (EOM) are described at first with reference to the G-system in figure 1, second the EOM are described with reference to the I-system. Only the dynamics of the mono-pile, i.e. from point E to point I, is considered in the EOM.

First the EOM for the (x_G, z_G) plane are derived, then in the (y_G, z_G) plane and finally torsion around the z_G-axis is considered.

$$m_i = \int_{-l_{EG}}^{l_{GI}} z_G^i\ \mu_s(z_G)\ dz_G \tag{25}$$

Thus e.g. m_0 is the total mass of the mono-pile.

EOM, (x_G, z_G) plane

Force equilibrium in the x_G direction with point G as reference

$$\int_{-l_{EG}}^{l_{GI}} \mu_s(z_G)\ \ddot{u}_{x_G}\ dz_G = -K_c^{(x)}(q_{x_G} - l_{CG}\ \theta_{y_G}) + \int_{-l_{EG}}^{l_{GI}} p_{wind}^{(x)}(z_G) + p_{wave}^{(x)}(z_G)\ dz_G + F_{x_I} \tag{26}$$

Inserting $\ddot{u}_{x_G} = \ddot{q}_{x_G} + z_G\ \ddot{\theta}_{y_G}$ in (26) one gets

$$\ddot{q}_{x_G}\ m_0 + \ddot{\theta}_{y_G}\ m_1 = -K_c^{(x)}\ (q_{x_G} - l_{CG}\ \theta_{y_G}) + \int_{-l_{EG}}^{l_{GI}} p_{wind}^{(x)}(z_G) + p_{wave}^{(x)}(z_G)\ dz_G + F_{x_I} \tag{27}$$

Force equilibrium in the z_G direction with point G as reference

$$m_0\ \ddot{q}_{z_G} = -\dot{q}_{z_G}\ C_{hd}^{(z)} - q_{z_G}\ \left(K_c^{(z)} + K_B^{(z)}\right) + F_{z_I} \tag{28}$$

Moment equilibrium in y_G direction with point G as reference

$$\int_{-l_{EG}}^{l_{GI}} \mu_s(z_G)\ \ddot{\alpha}_{y_G}\ dz_G = -\ K_{hs}^{(y)}\ \theta_{yG} - l_{CG}\ K_c^{(y)}\ (q_{x_G} - l_{CG}\ \theta_{y_G}) + \int_{-l_{EG}}^{l_{GI}} z_G\ \left(p_{wind}^{(x)}(z_G) + p_{wave}^{(x)}(z_G)\right)\ dz_G + l_{GI}\ F_{x_I} + M_{y_I} \tag{29}$$

Where $\ddot{\alpha}_{y_G} = z_G\ \ddot{u}_{x_G} = z_G\ \ddot{q}_{x_G} + z_G^2\ \ddot{\theta}_{y_G}$ - inserting this into (29) gives

$$m_1\ \ddot{q}_{x_G} + m_2\ \ddot{\theta}_{y_G} = -\ K_{hs}^{(y)}\ \theta_{y_G} - l_{CG}\ K_c^{(y)}\ (q_{x_G} - l_{CG}\ \theta_{y_G}) + \int_{-l_{EG}}^{l_{GI}} z_G\ \left(p_{wind}^{(x)}(z_G) + p_{wave}^{(x)}(z_G)\right)\ dz_G + l_{GI}\ F_{x_I} + M_{y_I} \tag{30}$$

EOM, (y_G, z_G) plane

Force equilibrium in the y_G direction with point G as reference

Analogue to (27)

$$\ddot{q}_{y_G}\ m_0 - \ddot{\theta}_{x_G}\ m_1 = -K_c^{(y)}\ \ (q_{y_G} + l_{CG}\ \theta_{x_G}) + \int_{-l_{EG}}^{l_{GI}} p_{wind}^{(y)}(z_G) + p_{wave}^{(y)}(z_G)\ dz_G + F_{y_I} \tag{31}$$

Moment equilibrium in x_G direction with point G as reference

$$m_1\ \ddot{q}_{y_G} - m_2\ \ddot{\theta}_{x_G} = -\ M_{hs} + l_{CG}\ K_c^{(x)}\ (q_{y_G} + l_{CG}\ \theta_{x_G}) + \int_{-l_{EW}}^{l_{WI}} z_G\ \left(p_{wind}^{(y)}(z_G) + p_{wave}^{(y)}(z_G)\right)\ dz_G + l_{GI}\ F_{y_I} + M_{x_I} \tag{32}$$

EOM, torsion in z_G-direction

$$I_t\ \ddot{\theta}_{z_G} = -K_{tc}\ \theta_{z_G} + M_{z_I} \tag{33}$$

Where I_t is the mass moment of inertia with respect to torsion. For a circular section with diameter, $D(z_G)$, and thickness, $t(z_G)$,

$$I_t = \frac{1}{2}\ \pi\ \rho_s \int_{-l_{EG}}^{l_{GI}} D(z_G)^2\ t(z_G)\ dz_G \tag{34}$$

A pre-assumption to (34) is that the mass moment contribution from the cables is ignorable.

6.4 EOM in matrix form

The "external" forcing terms in point I$(F_{x_I}(t), F_{y_I}(t), F_{z_I}(t), M_{x_I}(t), M_{y_I}(t), M_{z_I}(t))$ and in equations (7) and (9) may be collected and placed on the right hand side of the matrix form of the EOM and the equations in (27), (28), (30), (31), (32) and (33) can be collected into the left hand side in the matrix form of the EOM as follows

$$\mathbf{M}\ \ddot{\mathbf{q}}_\mathbf{G} + \mathbf{C}\ \dot{\mathbf{q}}_\mathbf{G} + \mathbf{K}\ \mathbf{q}_\mathbf{G} = \mathbf{F(t)} \tag{35}$$

In which the DOF vector is

$$\mathbf{q}_G = [q_{x_G}\ q_{y_G}\ q_{z_G}\ \theta_{x_G}\ \theta_{y_G}\ \theta_{z_G}]^T \tag{36}$$

the mass matrix

$$\mathbf{M} = \begin{bmatrix} m_0 & 0 & 0 & 0 & m_1 & 0 \\ 0 & m_0 & 0 & m_1 & 0 & 0 \\ 0 & 0 & m_0 & 0 & 0 & 0 \\ 0 & m_1 & 0 & m_2 & 0 & 0 \\ m_1 & 0 & 0 & 0 & m_2 & 0 \\ 0 & 0 & 0 & 0 & 0 & I_t \end{bmatrix} \tag{37}$$

the damping matrix

$$\mathbf{C} = \begin{bmatrix} 0 & 0 & 0 & 0 & 0 & 0 \\ 0 & 0 & 0 & 0 & 0 & 0 \\ 0 & 0 & C_{hd}^{(z)} & 0 & 0 & 0 \\ 0 & 0 & 0 & 0 & 0 & 0 \\ 0 & 0 & 0 & 0 & 0 & 0 \\ 0 & 0 & 0 & 0 & 0 & 0 \end{bmatrix} \tag{38}$$

and the stiffness matrix

$$\mathbf{K} = \begin{bmatrix} K_c^{(x)} & 0 & 0 & 0 & -l_{CG}\, K_c^{(x)} & 0 \\ 0 & K_c^{(y)} & 0 & l_{CG}\, K_c^{(y)} & 0 & 0 \\ 0 & 0 & K_c^{(z)} + K_B^{(z)} & 0 & 0 & 0 \\ 0 & l_{CG}\, K_c^{(y)} & 0 & K_{hs}^{(x)} + l_{BG}^2\, K_c^{(y)} & 0 & 0 \\ -l_{CG}\, K_c^{(x)} & 0 & 0 & 0 & K_{hs}^{(y)} + l_{BG}^2\, K_c^{(x)} & 0 \\ 0 & 0 & 0 & 0 & 0 & K_{tc} \end{bmatrix} \tag{39}$$

Finally, the force vector, $\mathbf{F}(t)$, is given by

$$\mathbf{F}(t) = \begin{bmatrix} \int_{-l_{EG}}^{l_{GI}} p_{wind}^{(x)}(z_G) + p_{wave}^{(x)}(z_G)\, dz_G + F_{x_I} \\ \int_{-l_{EG}}^{l_{GI}} p_{wind}^{(y)}(z_G) + p_{wave}^{(y)}(z_G)\, dz_G + F_{y_I} \\ F_{z_I} \\ \int_{-l_{EG}}^{l_{GI}} z_G \left(p_{wind}^{(y)}(z_G) + p_{wave}^{(y)}(z_G) \right) dz_G + l_{GI}\, F_{y_I} + M_{x_I} \\ \int_{-l_{EG}}^{l_{GI}} z_G \left(p_{wind}^{(x)}(z_G) + p_{wave}^{(x)}(z_G) \right) dz_G - l_{GI}\, F_{x_I} + M_{y_I} \\ M_{z_I} \end{bmatrix} \tag{40}$$

With the choices made in the subsection 2, the damping matrix in (38) is quite sparse. Other damping terms could have been quantified in subsection 2 - however a better approach for representing the system damping may be to apply a Rayleigh damping model

$$\mathbf{C} = \alpha\, \mathbf{M} + \beta\, \mathbf{K} \tag{41}$$

in which α and β are scalars that can be found based on guesses (or measurements) of the damping ratios, $\zeta^{(1)}$ and $\zeta^{(2)}$ of the two lowest modes. The lowest modes are expected to be fore-aft roll and side-side roll. Due to the symmetry of the mono-pile and the uncoupled dynamics between fore-aft and side-side roll - the two modes are expected to have equal natural frequency and damping, i.e. $\zeta^{(1)} = \zeta^{(2)}$.

The scalars in (41) can be found from, [13]

$$\begin{bmatrix} \alpha \\ \beta \end{bmatrix} = \frac{2\, \omega_1\, \omega_2}{\omega_2^2 - \omega_1^2} \begin{bmatrix} \omega_2 & -\omega_1 \\ -\dfrac{1}{\omega_2} & \dfrac{1}{\omega_1} \end{bmatrix} \begin{bmatrix} \zeta_1 \\ \zeta_2 \end{bmatrix} \tag{42}$$

ω_i the i'th cyclic/angular natural frequency, [rad/s]

6.5 Eigenvalue analysis

In this section, an eigenvalue solution to the un-damped (linear) eigenvalue problem is made for a specific parameterization - that is assuming a SWT 3.6 wind turbine located on top of a floating mono-pile (spar) with a diameter of 5m and a length of 135m as shown in figure 32) in subsection 6.12 and with key data given in table 6.5.

The following parameters are used for quantification of the eigenvalues and eigen vectors, note the parameters m_1 and m_2 are found with reference to point G (thus m_1 is practical zero) and for this example include the rotor/nacelle mass, m_n. The ballast is included by letting the mono-pile be massive at the lowest 5 meters, i.e. giving a ballast weight of 771 tons. The total weight, m_0, of wind turbine and mono-pile becomes 2476 tons which will submerge the mono-pile 123.0m when the weight of the mooring cables is not included and 124.4m when cable weight is included. The centre of gravity, point G, will be located 71.7m from the mono-pile bottom, point E. The cable support points (fairleads) are located 80m from the mono-pile bottom. In (43) below the eigenvalue

Table 4. Parameters for test mono-pile

Parameter name	Unit	Description	Value
m_n	[kg]	Total mass of rotor/nacelle	2.385 e+005
m_0	[kg]	Total mass (0th order mass moment)	2.4764e+006
m_1	[kg m]	1st order mass moment	5.9605e-008
m_2	[kg m2]	2nd order mass moment (mass moment of inertia in roll)	1.2622e+010
I_t	[kg m2]	Mass moment of inertia in torsion	2.7879e+006
$K_c^{(x)}$	[N/m]	Cable horizontal stiffness, x-dir	1.2606e+005
$K_c^{(y)}$	[N/m]	Cable horizontal stiffness, y-dir	1.2606e+005
$K_c^{(z)}$	[N/m]	Cable vertical stiffness	1.2606e+005
$K_B^{(z)}$	[N/m]	Vertical stiffness due to buoyancy	5.0276e+004
$K_{hs}^{(x)}$	[Nm/rad]	Water level hydrostatic stiffness due to fore-aft roll	6.9454e+006
$K_{hs}^{(y)}$	[Nm/rad]	Water level hydrostatic stiffness due to side-side roll	6.9454e+006
K_{tc}	[Nm/rad]	Cable stiffness due to torsion	6.6853e+005
l_{EB}	[m]	Distance point E to point B	72.6m
l_{BG}	[m]	Distance point B to point G	-0.9m
l_{GW}	[m]	Distance point G to point W	52.7
l_{WI}	[m]	Distance point W to point I	10.6
l_{IN}	[m]	Distance point I to point N (tower height)	68
D_w	[m]	Water depth	300

equation is given.

$$\left(\mathbf{K} - \omega_i^2\,\mathbf{M}\right)\ \mathbf{\Psi}_i\ ,\quad i = 1, 2..6 \tag{43}$$

Ψ_i the i'th eigen vector, [-]

Solving (43) with the matrices defined in (37) and (39) and parameterized as in table 6.5 one obtains the following eigenvalue results

Table 5. Natural frequencies of test configuration

Mode #	1	2	3	4	5	6
f_0, [Hz]	0.0037	0.0037	0.0362	0.0362	0.0425	0.0476

As seen the first modes have very low frequency with a time period of 270s! The two first modes are fore-aft and side-side modes, 3rd and 4th are fore-aft and side-side translatoric modes, 5th is heave mode and 6th is torsion mode.

The pre-stress force in the cables, $F_c^{(0)}$ has for the frequency results obtained in table 5.2 been set (quite arbitrary) to 89 kN (per cable) - if this number is change e.g. by a factor of 7 to 623 kN then the submerged depth becomes 132.5m, i.e. with only 2.5m from water surface level to interface, and the following natural frequencies are obtained

Table 6. Natural frequencies of test configuration

Mode #	1	2	3	4	5	6
f_0, [Hz]	0.0101	0.0101	0.0957	0.0954	0.0977	0.1258

As seen from table 6.5 the longest time period is now 99s!

If the logarithmic decrements, (δ_1, δ_2), for the two lowest modes (the rolling modes) are assumed equal to 0.1 - the damping scaling coefficients become α= 1.29e-4 and β= 7.88.

6.6 Dynamic couplings in the EOM

In the EOM as given in (35) the only coupling between the DOFs are through the relation given by the variable, $u_{x_G} = q_{x_G} + z_G\, \theta_{y_G}$. This coupling is causing the off-diagonal terms in both the mass matrix and the stiffness matrix. However, other couplings not yet included into the EOM exist, e.g.

- Roll and heave couplings: (θ_{x_G}, q_{z_G}) and (θ_{y_G}, q_{z_G})
- Roll and torsion couplings: $(\theta_{x_G}, \theta_{z_G})$ and $(\theta_{y_G}, \theta_{z_G})$

6.7 Roll and heave couplings

hold

6.8 Roll and torsion couplings

Inclusion of the roll-torsion coupling will have an effect on the mass moment of inertia in inertia and on the torsional stiffness due to tangential components from the cable forces. The modified to (33) EOM in torsion becomes

$$I_t\, \ddot{\theta}_{z_G} = K_{tc}\, \theta_{z,G} \tag{44}$$

In which

$$I_t = I_{t,0} + \left(\theta_{xy_G} \cdot z_G\right)^2 \cdot \rho_s \cdot \pi/4 \cdot D^2(Z_G) \tag{45}$$

where θ_{xy_G} is the resulting rotation from θ_{x_G} and θ_{y_G} and K_{tc} is given by (24). The relation between θxy_G, z_G, $\ddot{\theta}_{z_G}$ and θ_{zG} in (44) and (45) is non-linear.

6.9 Transformation of EOM from point G to point I

In this section the EOM given in (4) are transformed from point G to point I by the following linear transformation

$$\mathbf{q}_G = \mathbf{T} \cdot \mathbf{q}_I \tag{46}$$

Where

$$\mathbf{q}_I^T = [q_{I_x}\ q_{I_y}\ q_{I_z}\ \theta_{I_x}\ \theta_{I_y}\ \theta_{I_z}]\,,\ \mathbf{q}_G\text{is given by (36) and } \mathbf{T} = \begin{bmatrix} 1 & 0 & 0 & 0 & -l_{GI} & 0 \\ 0 & 1 & 0 & l_{GI} & 0 & 0 \\ 0 & 0 & 1 & 0 & 0 & 0 \\ 0 & 0 & 0 & 1 & 0 & 0 \\ 0 & 0 & 0 & 0 & 1 & 0 \\ 0 & 0 & 0 & 0 & 0 & 1 \end{bmatrix} \tag{47}$$

The first and second time derivatives of (46) are given by

$$\dot{\mathbf{q}}_G = \mathbf{T} \cdot \dot{\mathbf{q}}_I \tag{48}$$

$$\ddot{\mathbf{q}}_G = \mathbf{T} \cdot \ddot{\mathbf{q}}_I \tag{49}$$

To move the EOM with reference at one point to another point requires the mechanical energy of the system to be invariant to the transformation $\mathbf{T}$. Thus the potential,P_E, and kinetic,K_E, energies, general given by $P_E = 1/2\ \mathbf{q}^T\ \mathbf{K}\ \mathbf{q}$ and $K_E = 1/2\ \mathbf{q}^T\ \mathbf{M}\ \mathbf{q}$, must be equal in respectively the G- and I-system. This require the system matrices to transform according to the following $\mathbf{M}_I = \mathbf{T}^T\ \mathbf{M}_G\ \mathbf{T}$, $\mathbf{C}_I = \mathbf{T}^T\ \mathbf{C}_G\ \mathbf{T}$ and $\mathbf{K}_I = \mathbf{T}^T\ \mathbf{K}_G\ \mathbf{T}$, where indices I and G refer to the system for which the matrices correspond.

Hence the EOM in (refeq:dong:141) can be rewritten into the following

$$\mathbf{M}_I\ \ddot{\mathbf{q}}_I + \mathbf{C}_I\ \dot{\mathbf{q}}_I + \mathbf{K}_I\ \mathbf{q}_I = \mathbf{T}^T\ \mathbf{F} \tag{50}$$

6.10 Determination of optimal location of fairleads

Through a stochastic vibration analysis of the wind and wave loaded spar foundation the location of the fairleads (cable support points) resulting in the lowest fatigue loads is determined.

6.11 Appendix A

Determination of mooring cable horizontal and vertical stiffness
In this appendix the stiffness relation for one mooring cable is derived. In figure 31 below a sketch of the cable and the tensile force is shown.

Static equilibrium of the cable is given by

$$\frac{d}{ds}\left(F_c^{(x)}\ \frac{dy}{dx}\right) = w \tag{51}$$

where
w weight of cable pr. unit length, reduced for buoyancy
$F_c^{(x)}$ horizontal component of cable force

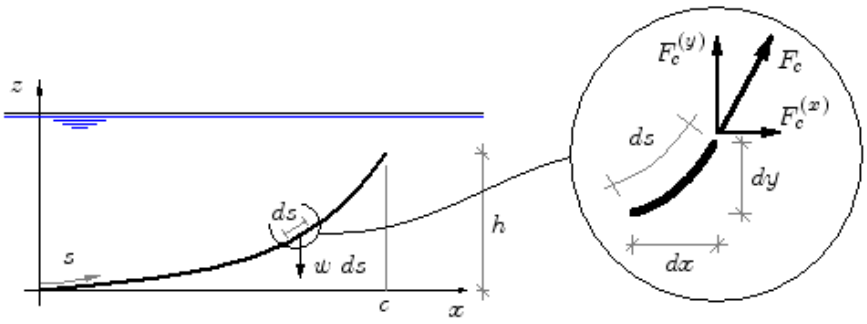

Figure 31. Mooring cable, geometry and tensile force

From figure 31 it can be found that

$$\frac{ds}{dx} = \sqrt{1 + \left(\frac{dy}{dx}\right)^2} \tag{52}$$

From (51) and (52) one gets

$$\frac{d^2y}{dx^2} = \lambda \sqrt{1 + \left(\frac{dy}{dx}\right)^2} \tag{53}$$

$$y(0) = \frac{dy(0)}{dx} = 0 \tag{54}$$

Where the wave length, λ, is given as $\lambda = \dfrac{w}{F_c^{(x)}}$

The solution to (53) is

$$y(x) = \frac{1}{\lambda}\ (\cosh(\lambda\ x) - 1) \tag{55}$$

For $x = c$: $y(c) = h$

$$h = \frac{1}{\lambda}\,(\cosh(\lambda\ c) - 1) \tag{56}$$

Horizontal stiffness
An increment, $\delta F_c^{(x)}$, of $F_c^{(x)}$ induces an increment, δc, of the cable span. The relation between these is derived by differentiation of (56) with regards to $F_c^{(x)}$

$$0 = -\frac{1}{\lambda^2}\,(\cosh(\lambda\ c) - 1)\,\frac{d\lambda}{dF_c^{(x)}} + \frac{1}{\lambda}\left(\sinh(\lambda\ c)\frac{d(\lambda c)}{dF_c^{(x)}} - \frac{\delta c}{\delta F_c^{(x)}}\right) \Rightarrow$$

$$\frac{\dfrac{1}{\lambda}\dfrac{w}{F_c^{(x)2}}\,(c\ \sinh(\lambda c) - h)}{\sinh(\lambda c) - 1} = \frac{\delta c}{\delta F_c^{(x)}} \Rightarrow$$

The spring constant of a single mooring cable thus becomes

$$k = \frac{\delta F_c^{(x)}}{\delta c} = \frac{\sinh(\lambda\ c) - 1}{\sinh(\lambda\ c) - \dfrac{h}{c}} \cdot \frac{F_c^{(x)}}{c} \tag{57}$$

The unknown, $F_c^{(x)}$, is determine next. The arc-length parameters $s(x)$ follows from (52) and (55)

$$s(x) = \int_0^x \sqrt{1 + \left(\frac{dy}{dx}\right)^2}\ dx = \int_0^x \cosh(\lambda\ x)dx = \frac{1}{\lambda}\sinh(\lambda\ x)$$

The length, l, of the cable follows for $x = c$. Then

$$\sinh(\lambda\, c) = \lambda\, l \tag{58}$$

For given c and l, (58) is solved iteratively for λ. With ω given, $F_c^{(x)}$ is determined from $\lambda = \dfrac{w}{F_c^{(x)}}$

Vertical stiffness
Pending

6.12 Appendix B

Test turbine, SWT/107/3.6MW with floating mono-pile substructure is shown in figure 32

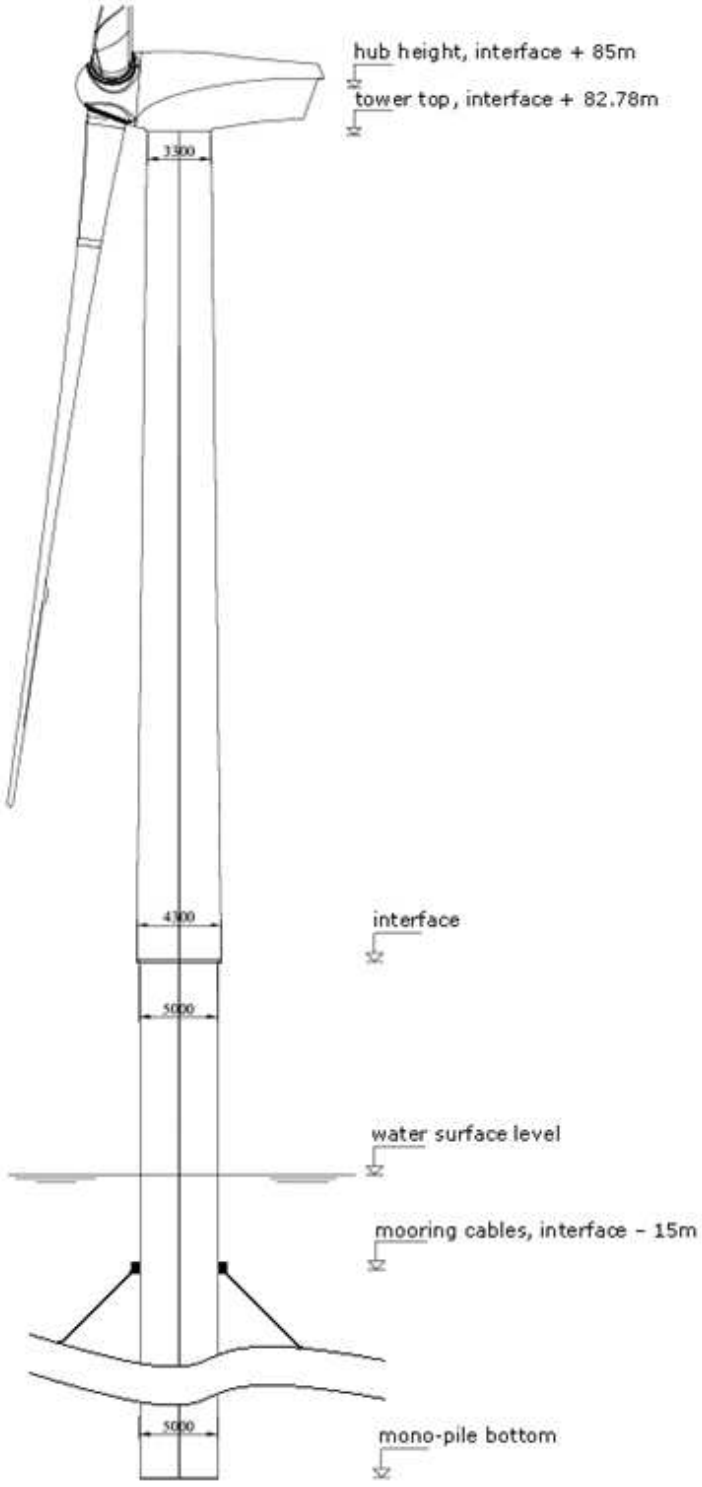

Figure 32. SWT/107/3.6MW with floating mono-pile substructure

7 Aero-Hydro-Elastic numerical simulation platform

By DHI

This section describes the work carried out to integrate Risø's aero-elastic code, HAWC2, with DHI's radiation/diffraction floating body analysis tool, WAMSIM.

Basically, HAWC2 models the wind turbines, while WAMSIM models the response in waves of the floating foundation.

7.1 HAWC2

The HAWC2 code is a code intended for calculating wind turbine response in time domain. The core of the code was mainly developed within the years 2003-2007 at the Aeroelastic Design research program at Risø-DTU.

The structural part of the code is based on a multibody formulation. In this formulation the wind turbine main structures is subdivided into a number of bodies where each body is an assembly of Timoshenko beam elements. Each body includes its own coordinate system with calculation of internal inertia loads when this coordinate system is moved in space, hence large rotation and translation of the body motion is accounted for. Inside a body the formulation is linear, assuming small deflections and rotations. This means that a blade modeled as a single body will not include the same nonlinear geometric effects related to large deflections as a blade divided into several bodies. The bodies representing the mechanical parts of the turbine are connected by joints also referred to as constraints. The constraints are formulated as algebraic equations that impose limitations of the bodies motion. This could in principal be a trajectory the body needs to follow, but related to the wind turbine implementation there are so far the possibility of a fixed connection to a global point (e.g. tower bottom clamping), a fixed coupling of the relative motion (e.g. fixed pitch, yaw), a frictionless bearing and a bearing where the rotation angle is controlled by the user. It may be worth to notice, that also for the last constraint where the rotation is specified, inertial forces related to this movement is accounted for in the response.

External forces are in general placed on the structure in the deformed state, which is especially important for pitch loads and twist of the blades and since large rotations are handled by a proper subdivision of bodies, the code is also especially suited for calculations on very flexible turbines subjected to e.g. large blade deflections. The aerodynamic part of the code is based on the blade element momentum theory, but extended from the classic approach to handle dynamic inflow, dynamic stall, skew inflow, shear effects on the induction and effects from large deflections. One example is the effect of large flapwise blade deflections causing a change in the effective rotor diameter and that the blade forces are no longer perpendicular to the rotor plane. This reduces the thrust on the rotor thereby changing the induced velocities and vice versa.

Two dynamic stall models have been implemented where the first is generally known as the Øye model, which includes the effect of stall separation lag. The second model is a modified Beddoes-Leishmann model that includes the effects of shed vorticity from the trailing edge (Theodorsen Theory), as well as the effects of stall separation lag caused by an instationary trailing edge separation point. These effects are especially important

related to flutter analysis, but also generally to calculate loads and stability of blades with very low torsion stiffness.

The wind conditions are divided into deterministic and stochastic wind. The deterministic wind is mean wind velocity, wind steps, ramps, special gust events, special shears including the possibility for fully user defined shears. The stochastic wind normally referred to as turbulence is generated outside the HAWC2 code. In the HAWC2 code two formats for reading turbulence data are possible. One is in Cartesian coordinates (e.g. Mann turbulence generated by the code WAsP engineering) and the other is in polar coordinates (the Veers model used by FLEX5). Tower shadow effects are also a part of the wind module as it changes the wind conditions locally near the tower. For upwind turbines a potential flow method is used whereas a jet-model produces much better results for downwind turbines.

Control of the turbine is performed through one or more DLLs. The format for these DLLs is very general, which means that any possible output sensor normally used for data file output can also be used as a sensor to the DLL. This allows the same DLL format to be used whether a control of a bearing angle, an external force or moment is submitted to the structure. The default controller supplied with code is an open source DLL including a pitch regulated variable speed controller.

7.2 WAMSIM

The radiation/diffraction code WAMSIM for calculating floating body dynamics is based on the frequency-domain program WAMIT for the calculation of the hydrodynamic quantities [5, 6, 14]. The following short general description of WAMSIM is taken from [14]; The hydrodynamic interaction between the fluid and floating bodies is assumed to be well described by linear potential theory (i.e. an inviscid and irrotational flow, with the free surface and body boundary conditions satisfied to first order). That is to say, de-spite any non-linear effects, which may have been important in producing the conditions at the bodies; all non-linear terms are ignored in the free surface boundary conditions in the local vicinity of the bodies, as well as in the expressions for fluid pressure and force on the bodies. This is a good approximation as long as the parameter $kH/\tanh(kh) << 1$ Assuming the body motions remain small, the equations of motion for the body dynamics for the N degrees of freedom can be written in the following convolution form:

$$\sum_{k=1} N \left[(M_{jk} + a_{jk})\, \ddot{x}_k(t) + \int_0^t K_{jk}(t-\tau) \cdot \dot{x}_k(\tau) \mathrm{d}\tau + C_{jk} x_k(t) \right] = F_{jD}(t) + F_{jnl}(t), \quad j = 1, 2, \ldots, N \tag{59}$$

All non-linear external forces, such as those due to the mooring system or possibly viscous/frictional damping, are included via the term $F_{jnl}(t)$. The rest of this equation de-scribes the inertia, hydrostatic, and hydrodynamic forces on the bodies to first order in the body motion and the wave steepness.

The bodies' linear inertia and hydrostatic restoring matrices are M_{jk} and C_{jk}, respectively. The forces due to radiated waves generated by the bodies' motions are expressed as a convolution of the radiation impulse response functions, K_{jk}, with the body velocity, $\dot{x}_k$, (plus the impulsive contributions, a_{jk}, which come from the $t = 0$ limit of the radiation problem, and are proportional to acceleration).

The wave exciting force, $F_{jD}(t)$, is obtained from the Haskind relations, which express the diffraction force in terms of solutions to radiation problems:

$$F_{jD}(t) = \int\int_{S_0} p_I(\vec{x},t) \cdot n_j(\vec{x}) \mathrm{d}\vec{x} + \rho \int_{-\infty}^{\infty} \left(\int\int_{S_0} \phi_j(\vec{x}, t-\tau) \dot{\phi}_{In}(\vec{x},\tau) \mathrm{d}\vec{x} \right) \mathrm{d}\tau \quad (60)$$

In Equation (60), ϕ_I is a known incident wave potential, which satisfies the linear free surface boundary condition and induces a first order dynamic pressure $p_i = -\rho \frac{\partial \phi_i}{\partial i}$ in the fluid.

7.3 Coupling of HAWC2 with WAMSIM

The coupling of the models has been performed by letting a special version of WAMSIM interact with an interface for external models included in HAWC2. The special WAMSIM model has been compiled as a dynamically linked library (dll) that is activated and controlled by HAWC2. A number of modifications has been made to WAMSIM in order to return the right quantities to HAWC2 at the right times.

The coupled model involves the following steps:

1. Mass matrices and stiffness matrices of the floating foundation are calculated by WAMSIM and delivered to HAWC2
2. HAWC2 sets up mass and stiffness matrices for the entire system including wind turbines and floating foundation.
3. The simulation is initiated by HAWC2. A WAMSIM subroutine is called by HAWC2, with HAWC2's guess on the state of the system (ie. velocities and position in 6 DOF's) and the constraint force at the model interface (ie. forces from wind turbines on foundation). The subroutine uses parts of the WAMSIM routine for solving body equations of motion to returns the state differentiated with respect to time (ie. accelerations and velocities). All hydrodynamics incl. added mass and forcing from incident waves are included in this step. Restor-ing forces from a mooring system set up in WAMSIM are also taken into account.
4. The iterative solver of HAWC2 will repeat Step 3 with new guesses of the state vector until the calculated residuals are acceptable. When the acceptance criteria are met it will proceed to the next time step, and step 3 is repeated for this time step.

7.4 Model Verification

A number of simulations have been carried out to validate the coupled model. Motions calculated by the coupled model, ie. by HAWC2's motion equation solver, are com-pared to motions calculated by a standard stand-alone version of WAMSIM. The former results (termed WAMSIM dll) are shown with a thin red line and the latter with a thicker black line (WAMSIM exe) in the following figures.

The validation runs have been carried out for a floating box of 50x20x3 m with the centre of gravity of the floating box in the water surface. The coordinate system is defined as a right hand Cartesian coordinate system with origo in the centre of gravity of the box and with z pointing upwards. A soft linear mooring system is applied to the box to obtain some restoring force in the lateral modes (surge, sway and yaw). Otherwise, small numerical noise would build up and eventually cause large motions

in these modes, as if the box were drifting away. The mooring system is modelled by WAMSIM's built-in mooring system module for both the coupled and the stand-alone model.

The first validation run (Figure 33) is a simple decay test in with only the floater having a mass. The floater is given an initial 1 m heave, 5^O roll and 2^O pitch and. The HAWC2 and the WAMSIM solvers are seen to produce identical results for this case.

Validation runs shown in Figure 34 to Figure 42 all include a concentrated mass of 10^6 kg. In the coupled model (WAMSIM dll) this is simulated by HAWC2 as a concentrated mass at the end of an infinitely stiff beam. In the WAMSIM stand-alone it is simulated by modifying the mass matrix accordingly A short description of the validation runs and their motivation is given here;

Figure 34: The concentrated mass is placed 2 meter above the centre of gravity. An initial roll displacement is allowed to decay without any external (wave) forcing. The external mass also produces a 1 meter downward displacement of the box as expected. There is good agreement between the models for the relevant modes (sway, heave and roll). The discrepancy in sway may be contributed to the fact that the HAWC2 solver produces a little bit of initial flutter - seen by the fact that the initial sway is not exactly equal to zero.

Figure 35: : Identical to Figure 34 except that an initial pitch of 2^O is also given. Small discrepancies in surge and sway are observed. Again these are contributed to the initial flutter produced by HAWC2 before it becomes stable after a couple of seconds.

Figure 36 and Figure 37: Same position of the concentrated mass as above. No initial displacement given, except for a 1 m downwards movement (corresponding to the displacement caused by the concentrated mass). The box is exposed to irregular waves with Hm0 = 0.5m and Tp = 3.6s approaching at an angle of 45 to the box. The concentrated mass has not been included in the WAMSIM stand-alone solver in Figure 36, while it has been included in Figure 37. The effect is clearly seen. The two solvers produce very similar results when the concentrated mass is included in both.

Figure 38 to Figure 39: The concentrated mass is placed 10 meter above the water surface and 1 m away from the centreline, whereby it should produce a resultant roll moment. A simulation without waves (Figure 38) and a simulation with waves (Figure 39) have been made. The solvers give very similar results and reproduce the same roll-induced sway motions.

Figure 40 to Figure 42: The concentrated mass is placed 10 meter above the water surface at position (x,y) = (4m,1m), and will therefore produce both roll and pitch moments. A simulation without waves (Figure 2.8) and two wave simulations (Figure 41 and Figure 42) have been made. There is generally good agreement between the two solvers. The largest discrepancies are found for yaw motions, where the coupled solver is producing motions about twice as large as the WAMSIM stand-alone solver when the forcing is small (Figure 40 and Figure 41). This may be caused by limitations in the way the WAMSIM stand-alone version handles the effect of the concentrated mass. The static weight of the concentrated mass is applied as a constant downward force in (x,y) = (4m,1m). The point of attack of this force relative to the coordinate system origo is not updated according to the displacement of the floating body. Hence, when there are relatively large roll and pitch rotations, the WAMSIM stand-alone may underestimate the actual contribution from the concentrated mass to the yaw movement

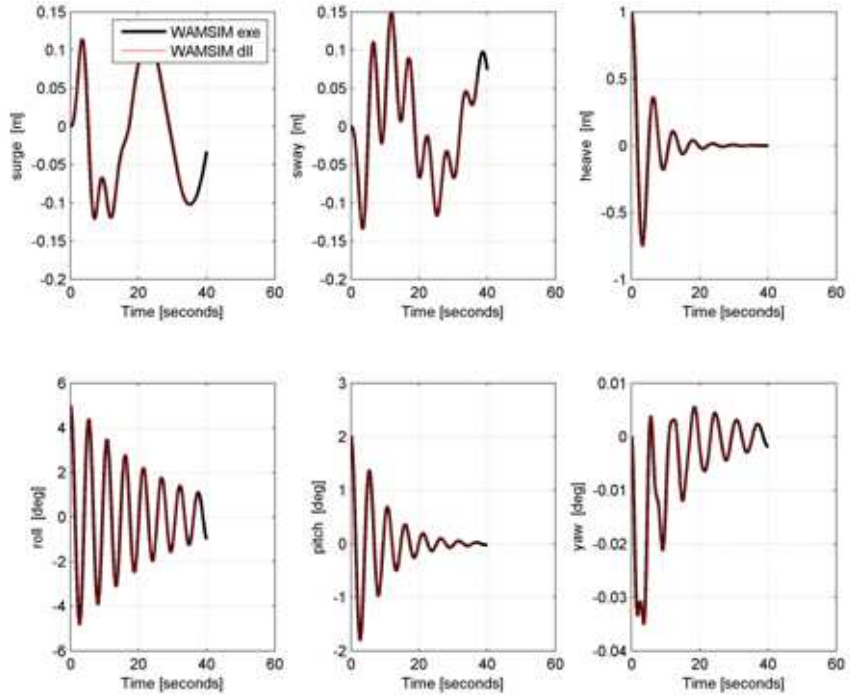

Figure 33. Decay Test - Floating Box only

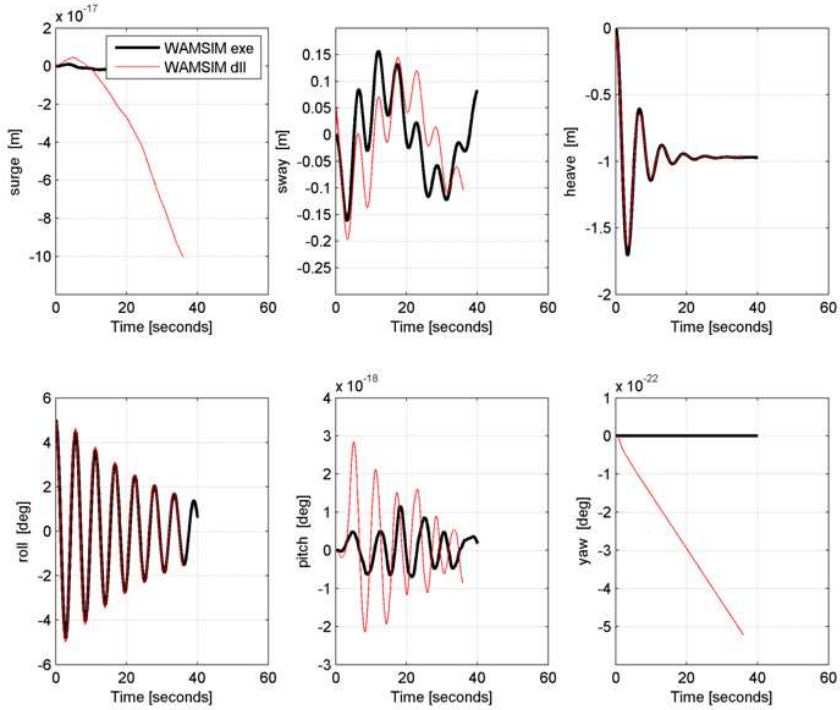

Figure 34. (x,y,z)-mass = (0,0,2m). 5^O initial roll

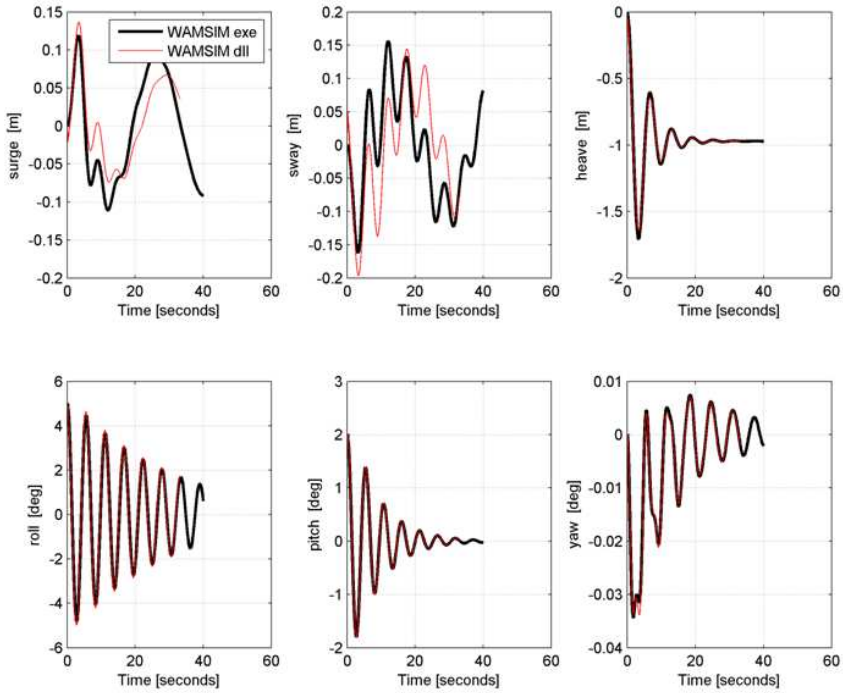

Figure 35. (x,y,z)-mass = (0,0,2m). 5^O initial roll, 2^O initial pitch

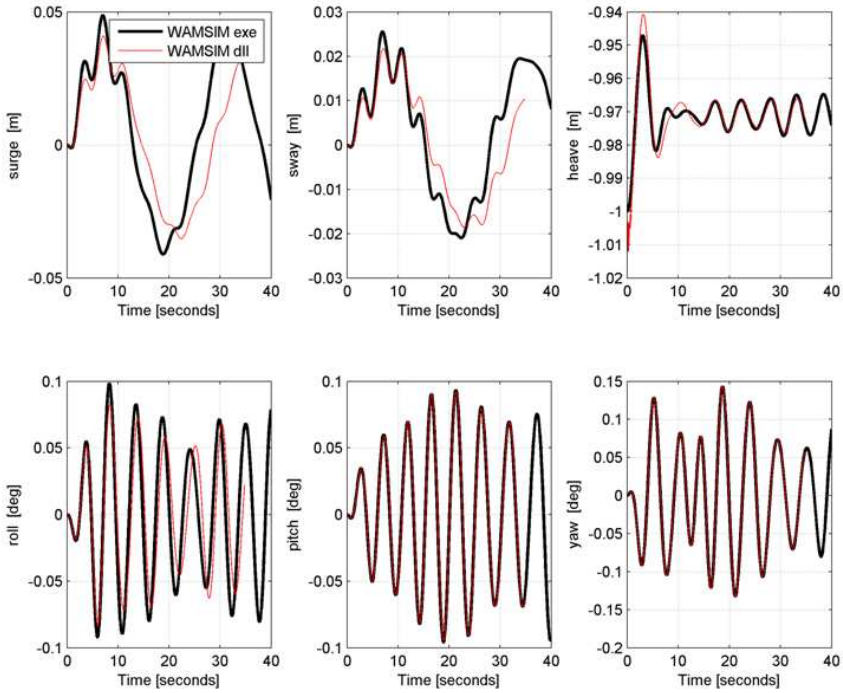

Figure 36. (x,y,z)-mass = (0,0,2m) - wave forcing - conc. mass not included in wamsim.exe model

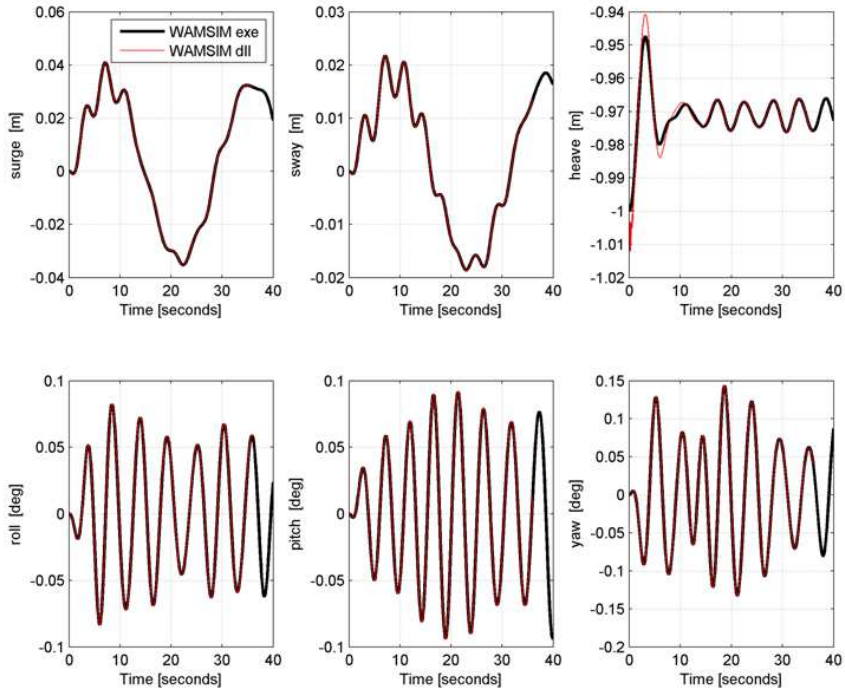

Figure 37. (x,y,z)-mass = (0,0,2m) - wave forcing - conc. mass <u>included</u> in wamsim.exe model

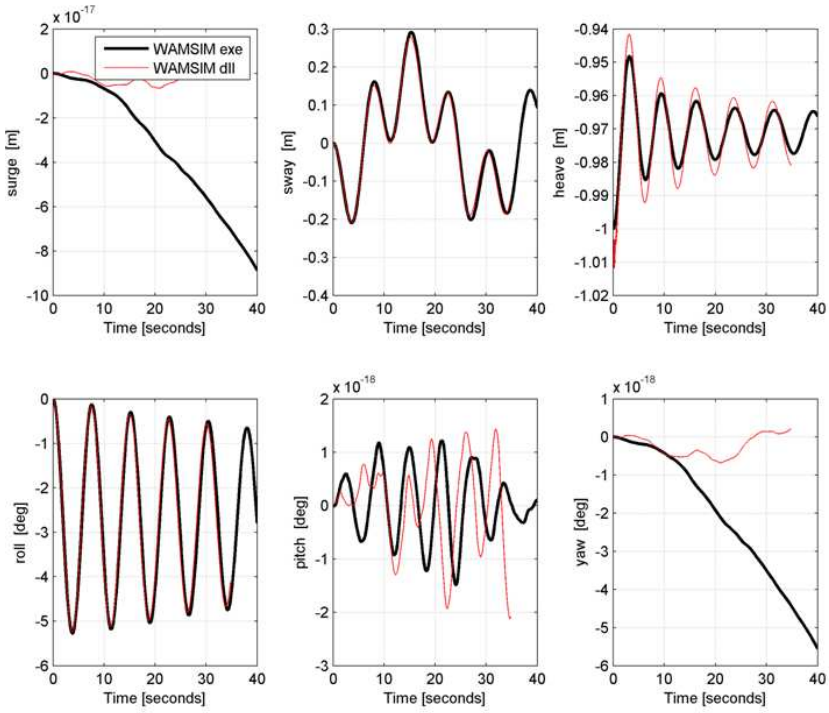

Figure 38. (x,y,z)-mass = (0,1m,10m) - no wave forcing

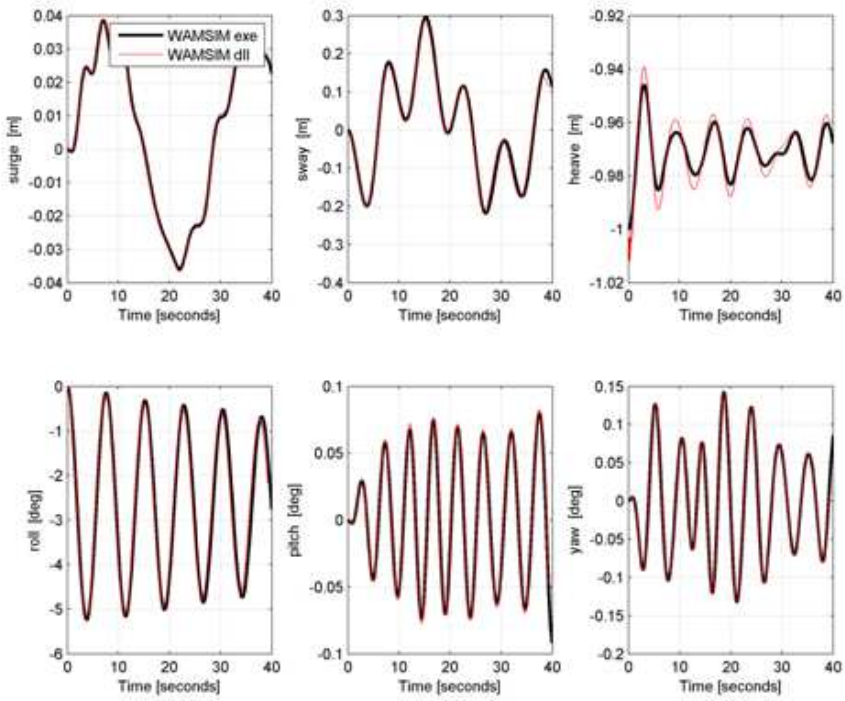

Figure 39. x,y,z)-mass = (0,1m,10m) - incl. wave forcing

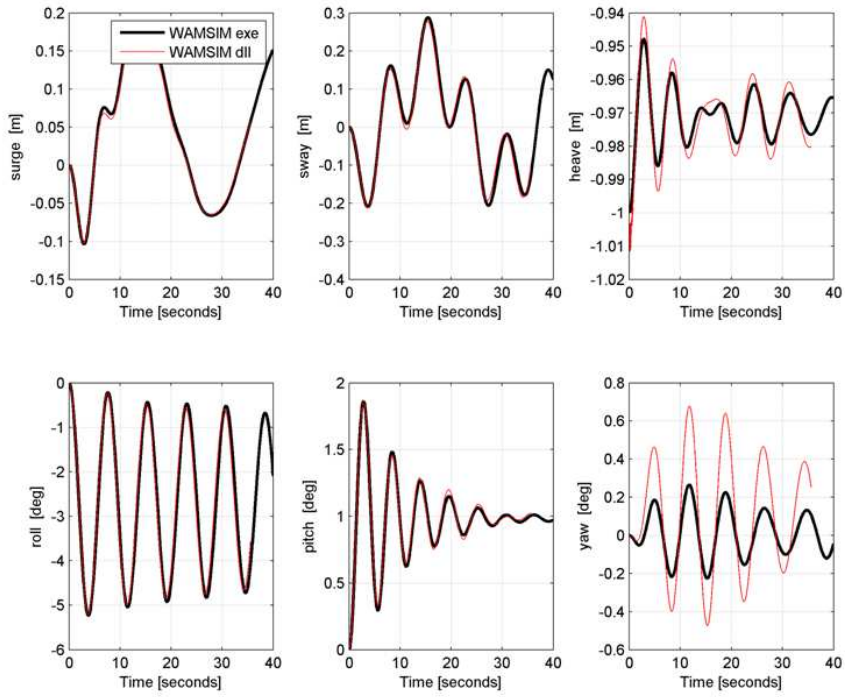

Figure 40. (x,y,z)-mass = (4m,1m,10m) - no wave forcing

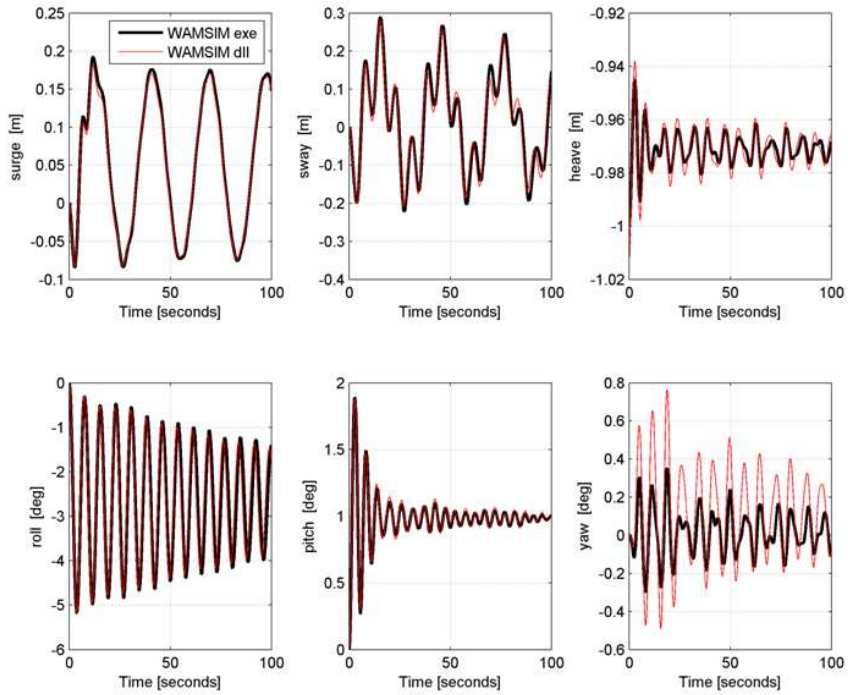

Figure 41. (x,y,z)-mass = (4m,1m,10m) - wave forcing - H_s=0.5m, T_p=3.6s

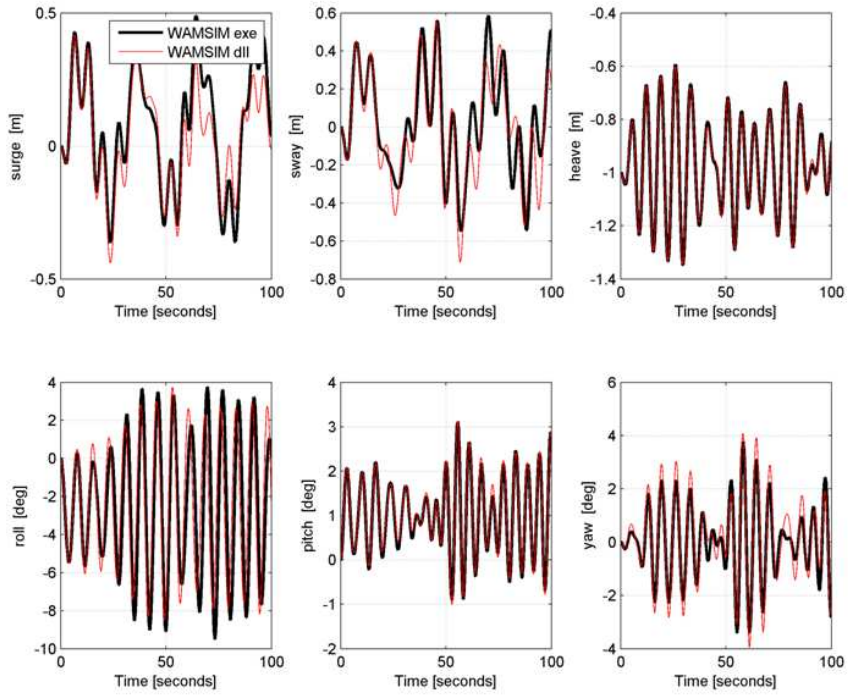

Figure 42. (x,y,z)-mass = (4m,1m,10m) - wave forcing - H_s=1.8m, T_p=6.5s

References

[1] Making waves. *Economist*, 379.

[2] A. Muetze and J. G. Vining. Ocean wave energy conversion - a survey. In *Proc. Industry Applications Conference 8-12 Oct. 2006*, pages 1410–1417, 2006.

[3] http://peswiki.com/energy/directory:ocean_wave_energy.

[4] C. P. Butterfield, W. Musial, and J. Jonkman. Overview of offshore wind technology. *NGCWP 2007 - Proceedings of 2007 Non-Grid-Connected Wind Power Systems - Wind Power Shanghai 2007 - Symposium on Non-Grid-Connected Wind Power*, pages 419–427, 2007.

[5] H. B. Bingham. A hybrid boussinesq-panel method for predicting the motion of a moored ship. *Coastal Engineering, volume = 40, pages = 21–38, year = 2000,*.

[6] E. D. Christensen, B. Jensen, S. Mortensen, H. F. Hansen, and J. Kirkegaard. Numerical simulation of ship motion in offshore and harbour areas. In *Proc. ASME 27th Int. Conf. on Offshore Mechanics and Arctic Engineering*, Estoril, Portugal, 2008.

[7] T. J. Larsen and T. D. Hanson. A method to avoid negative damped low frequent tower vibrations for a floating, pitch controlled wind turbine. *Journal of Physics: Conference Series*, 75(1):012073–1–11, 2007.

[8] F. Rasmussen and A. Kretz. Dynamics of a two-bladed teetering rotor. Risø-r-1073(en), RisøNational Laboratory, 1992.

[9] P. Vølund and F. Rasmussen. Designverifikation for fleksibel to-bladet møller. Risø-r-617(en), RisøNational Laboratory, 1999.

[10] T. J. Larsen (Editor). How 2 HAWC2, the user's manual. Risø-r-1597(ver. 3-7)(en), RisøNational Laboratory, 2009.

[11] et al. T. Ishihara. A numerical study on the dynamic response of a floating offshore wind turbine system due to resonance and nonlinear wave.

[12] et al. A. Knauer. Simulation of floating wind turbine concept.

[13] S. R. K. Nielsen. *Svingningsteori, bind 1, Liner svingningsteori*. Aalborg tekniske universitetsforlag (in Danish).

[14] H. F. Hansen, S. Carstensen ans E. D. Christensen, and J. Kirkegaard. Multi vessel inter-action in shallow water. In *OMAE2009-79161, Proc. ASME 28th Int. Conf. on Offshore Mechan-ics and Arctic Engineering*, Honolulu, Hawaii, USA., 2008.

Risø DTU is the National Laboratory for Sustainable Energy. Our research focuses on development of energy technologies and systems with minimal effect on climate, and contributes to innovation, education and policy. Risø DTU has large experimental facilities and interdisciplinary research environments, and includes the national centre for nuclear technologies.

Risø DTU
National Laboratory for Sustainable Energy
Technical University of Denmark

Frederiksborgvej 399
PO Box 49
DK-4000 Roskilde
Denmark
Phone +45 4677 4677
Fax +45 4677 5688

www.risoe.dtu.dk

Risø-R-1767(EN)